ISSN/2499-5347

E. NICHELATTI
Nuclear Department
Physical Technologies and Safety Division
Particle Accelerator Laboratory
Casaccia Research Center

C. RONSIVALLE, M.D. ASTORINO, G. BAZZANO, P. NENZI, V. SURRENTI
Nuclear Department
Physical Technologies and Safety Division
Particle Accelerator Laboratory
Frascati Research Center

THE TOP-IMPLART HIGH-ENERGY PROTON BEAM DELIVERY LINE: A COMPARISON OF SRIM, FLUKA, AND FERMI-EYGES THEORY PREDICTIONS

RT/2025/6/ENEA

ENEA
ITALIAN NATIONAL AGENCY FOR NEW TECHNOLOGIES, ENERGY AND SUSTAINABLE ECONOMIC DEVELOPMENT

E. NICHELATTI

Nuclear Department
Physical Technologies and Safety Division
Particle Accelerator Laboratory
Casaccia Research Center

C. RONSIVALLE, M.D. ASTORINO,
G. BAZZANO, P. NENZI, V. SURRENTI

Nuclear Department
Physical Technologies and Safety Division
Particle Accelerator Laboratory
Frascati Research Center

THE TOP-IMPLART HIGH-ENERGY PROTON BEAM DELIVERY LINE: A COMPARISON OF SRIM, FLUKA, AND FERMI-EYGES THEORY PREDICTIONS

RT/2025/6/ENEA

ITALIAN NATIONAL AGENCY FOR NEW TECHNOLOGIES,
ENERGY AND SUSTAINABLE ECONOMIC DEVELOPMENT

THE TOP-IMPLART HIGH-ENERGY PROTON BEAM DELIVERY LINE: A COMPARISON OF SRIM, FLUKA, AND FERMI-EYGES THEORY PREDICTIONS

E. Nichelatti, C. Ronsivalle, M.D. Astorino, G. Bazzano, P. Nenzi, V. Surrenti

Abstract
In the framework of the TOP-IMPLART project, a beam delivery line has been designed and is under commissioning for the TOP-IMPLART proton linear accelerator to enable irradiation scans of extended targets at energies of 63 and 71 MeV. To suitably plan these irradiations, it is necessary to know the lateral size and angular spread of the beam arriving at the target plane. In a preliminary stage, this evaluation can be performed using simulations and theoretical models. In this Technical Report, we examine the current design of the TOP-IMPLART beam delivery line using two Monte Carlo codes, SRIM and FLUKA, as well as a numerical approach based on the Fermi-Eyges theory. The results show that SRIM underestimates the beam's lateral size and angular spread of the beam at the target plane compared to FLUKA. An experimental test confirms that SRIM underestimates the spot size, while FLUKA is in good agreement with the experiment. The predictions of the Fermi-Eyges theory are closer to the results provided by FLUKA.

Keywords: *proton beam, linear accelerator, TOP-IMPLART, Monte Carlo simulation, SRIM, FLUKA, beam emittance, Fermi-Eyges theory.*

Riassunto
Nell'ambito del progetto TOP-IMPLART, è stata progettata ed è in fase di "commissioning" una linea di rilascio del fascio per l'acceleratore lineare di protoni TOP-IMPLART dedicata a irraggiamenti a scansione di bersagli estesi a energie di 63 e 71 MeV. Per pianificare adeguatamente tali irraggiamenti, è necessario conoscere la dimensione laterale e la dispersione angolare del fascio che arriva sul piano del bersaglio. In una fase preliminare questa valutazione può essere eseguita utilizzando simulazioni e modelli teorici. In questo Rapporto Tecnico, esaminiamo il progetto attuale della linea di trasporto del fascio TOP-IMPLART utilizzando due codici Monte Carlo, SRIM e FLUKA, nonché un approccio numerico basato sulla teoria di Fermi-Eyges. I risultati mostrano che SRIM sottostima la dimensione laterale e la dispersione angolare del fascio sul piano del bersaglio rispetto a FLUKA. Un test sperimentale conferma che SRIM sottostima la dimensione del fascio, mentre FLUKA è in buon accordo con l'esperimento. Le previsioni della teoria di Fermi-Eyges sono più vicine ai risultati forniti da FLUKA.

Parole chiave: fascio di protoni, acceleratore lineare, TOP-IMPLART, simulazione Monte Carlo, SRIM, FLUKA, emittanza del fascio, teoria di Fermi-Eyges.

INDEX

1. Introduction

The TOP-IMPLART linac is a pulsed radiofrequency proton linear accelerator in operation at the ENEA Frascati Research Center. It delivers a 71 MeV proton beam in pulses that are 2.5 μs long, with a typical repetition frequency of 25 Hz. It consists of a 7 MeV injector operating at 425 MHz, followed by a booster composed of eight SCDTL (Side Coupled Drift Tube Linac) modules operating at 3 GHz. The accelerator is equipped with two extraction lines: a low-energy (1-6 MeV) vertical extraction line at the injector output, and a high-energy (63-71 MeV) 2.7-m long horizontal line after the booster. The maximum output energy is 71 MeV, but a second output energy of 63 MeV can be obtained by switching-off the radiofrequency field in the last accelerating module. Intermediate and lower energies are available using beam energy degraders.

The accelerator, originally designed as the first prototype of a protontherapy system based on a full linear layout, is part of the TOP-IMPLART project (Terapia Oncologica con Protoni – Intensity Modulated Proton Linear Accelerator for RadioTherapy). This project is funded by Regione Lazio (Italy) and conducted by ENEA in collaboration with ISS (Istituto Superiore di Sanità – Italian National Institute of Health) and Hospital Regina Elena-IFO. It has promoted the development of engineered versions based on this innovative scheme [Rons2011, Pica2020, Nenz2022]. Presently, due to the growing interest in a proton beam with the characteristics of TOP-IMPLART in various fields of application, significant efforts are being made to evolve the prototype into a facility available for research and industrial users.

The horizontal line includes a scanning magnetic system to irradiate extended targets up to 10x10 cm^2. It also features several tools to monitor parameters of interest, such as dose, fluence, and flux. The beam exits the last accelerating module (SCDTL-8) and passes through a short extraction line with two PMQs (Permanent Magnet Quadrupoles), ending with a 25 μm titanium (Ti) window. The beam then travels through 13 cm of air before entering the delivery pipe. To reduce beam scattering, the delivery pipe is filled with helium (He). The beam exits the delivery pipe and propagates in air to the irradiation station where the target is placed. A detailed description of this line can be found in [Surr2023]. The design of the irradiation station is based on a versatile layout capable of defining custom irradiation setups. It is equipped with actuators and mechanical supports, an ionization chamber for irradiation verification and dosimetry, a range shifter and collimators, and X-Y actuators for irradiation frame positioning.

In order to plan irradiations, it is essential to know the characteristics of the transported proton beam at the target plane, specifically its lateral size, shape, angular divergence, and energy spectrum. In other words, the phase space characteristics of the beam at the target plane. This knowledge will also aid in making decisions about the best setup (position of target, collimator size, absorber thickness, etc.) to satisfy user requirements. An evaluation of these beam characteristics can be done using simulation programs, such as Monte Carlo (MC) codes, or numerically through suitable particle transport theories.

For this purpose, we consider the two well-known MC codes SRIM [Zieg2008, Zieg2010, Srim2013] and FLUKA [Ferr2005, Vlac2009, Böhl2014, Batt2015, Ahdi2022, Fluk2025], as well as the Fermi-Eyges (FE) theory of particle transport [Ross1941, Eyges1948], using a differential form of the scattering power developed by Gottschalk [Gott2010, Gott2012]. We apply these approaches to two distinct cases of 63 and 71 MeV proton beams, whose phase-space particle distributions at the linac exit are simulated using LINAC software [Cran1994]. The results of the beam propagation characteristics obtained with these three approaches are compared. A comparison between an experimentally measured beam spot size at the energy of 71 MeV in the TOP-IMPLART linac and the results provided by these MC codes and the FE theory is also shown.

2. Three approaches to the transport of proton beams

The transport of a proton beam along a delivery line that includes different materials is a complex phenomenon. The accelerated protons experience elastic and anelastic interactions with the material atoms along their path. Due to these interactions, the protons lose part of their kinetic energy and, at the same time, undergo multiple Coulomb scattering (MCS) events that cause random angular deflections of their trajectories. The result of these phenomena is a progressive reduction in the beam's mean energy and an enlargement of its transverse dimension. Generally, the increasingly enlarging transverse shape of such a beam is only approximately Gaussian. However, it can be considered Gaussian to a very good degree of approximation once a minor external halo contribution is neglected.

Here, we briefly recall the main concepts of three different approaches to the propagation of a proton beam. While the first two approaches use MC simulations for beam transport, the third relies on the numerical evaluation of specific formulas.

2.1 SRIM simulation software

SRIM (Stopping and Range of Ions in Matter) is a suite of software programs to simulate the interaction of ions with matter [Zieg2008, Zieg2010, Srim2013]. Developed by James F. Ziegler, it is freely available for non-commercial use. The programs simulate the penetration of ions into solid, liquid, and gaseous targets, providing detailed information about the ion's trajectory, energy loss, and the resulting damage to the target material. An MC approach is used for the ion trajectory computations. SRIM has a relatively simple and intuitive interface, making it easily accessible to researchers and students. In this Technical Report, version 2013 of SRIM was used.

SRIM is based on approximations of the Bethe-Bloch and Lindhard-Scharff-Schiøtt theories to describe the energy loss of ions due to electronic excitations and nuclear collisions in the target material, respectively. The program is a binary collision approximation (BCA) MC code and uses several physical approximations to enhance computational efficiency. The most important ones are the use of an analytical formula for the evaluation of atom-atom scattering and the concept of free flightpaths between collisions. After each two-body collision, the distance to the next one and its impact parameter are chosen randomly using a probability distribution. The energetic ion is assumed to lose energy only along the free paths between collisions due to electronic stopping power, with no energy lost when colliding with nuclei. Moreover, only significant collisions are considered, while minor collisions are skipped. Regarding multiple scattering, SRIM implements the Lindhard-Nielsen approach, but uses the Ziegler-Biersack-Littmark interatomic potential in place of the Thomas-Fermi one.

2.2 FLUKA simulation software

FLUKA (FLUktuierende KAskade) is a powerful, general-purpose MC simulation program designed to model the transport and interaction of particles and nuclei with matter [Ferr2005, Vlac2009, Böhl2014, Batt2015, Ahdi2022, Fluk2025]. Starting with a pioneering code developed by Johannes Ranft in 1970 for hadronic cascades, and followed by a second-generation version created in collaboration with Pertti Aarnio, Alberto Fassò, Hans-Joachim Moehring, and Graham Stevenson, the modern third-generation version of FLUKA has been developed by Alberto Fassò, Alfredo Ferrari, Johannes Ranft, and Paola Sala, with contributions from numerous other scientists over the years. It is currently maintained and distributed by INFN (Istituto Nazionale di Fisica Nucleare, Italy) and CERN (European Council for Nuclear Research). FLUKA is freely available for non-commercial use, and the latest versions can be downloaded from the official FLUKA websites hosted by INFN [Fluk2025b] and CERN [Fluk2025]. It is

a fully integrated tool, handling all stages of particle transport, from initial interactions to the tracking of secondary particles. In this Technical Report, CERN's version 4-4.1 of FLUKA was used [Fluk2025] along with version 3.3-1 of its graphical user interface, Flair [Vlac2009].

FLUKA uses MC methods to simulate the transport of particles through matter, taking into account scattering, energy loss, and other processes. It implements Molière's theory for multiple scattering of ions in matter [Moli1947, Moli1948, Beth1953], provided that the elementary number of scattering events is large enough (greater than 20, otherwise single-scattering algorithms can be used). The underlying single-scattering cross section is the Rutherford one, corrected for screening. FLUKA incorporates various models to describe nuclear reactions, including the cascade model for high-energy interactions and the evaporation model for low-energy interactions. The simulation of electromagnetic processes, such as ionization and Bremsstrahlung, is based on well-established theories like the Bethe-Bloch equation.

FLUKA is known for its high accuracy in simulating a wide range of particle interactions, thanks to its sophisticated models and extensive validation. The code can handle a broad spectrum of particles, energies, and materials, making it suitable for diverse applications. It provides a complete set of tools for simulating particle transport, including geometry definition, material specification, and scoring of desired quantities. The FLUKA development team continuously updates and improves the code, incorporating new models and features.

Overall, FLUKA is a powerful and widely used tool for simulating particle transport and interactions. Its accuracy, versatility, and comprehensive features make it a valuable asset in various scientific and engineering disciplines. However, FLUKA can be challenging to learn and use, especially for beginners, due to its complex input format and numerous options. While it has a basic geometry visualization tool, it may not be as user-friendly as some other simulation packages. The complexity of FLUKA and its computational demands require careful consideration and expertise for effective utilization.

2.3 Fermi-Eyges theory

The FE theory, developed by Enrico Fermi [Ross1941] and later extended by Leonard Eyges [Eyge1948], describes the multiple scattering and propagation of charged particles as they traverse matter. It involves the use of phase-space diagrams to visualize correlations between position and direction in a particle beam. At its core, the theory assumes that the scattering angles are small, and the energy loss of particles is treated as a continuous process (CSDA, continuous slowing down approximation) rather than employing discrete collisions. The angular distribution of the scattered particles is approximated as Gaussian, and the same is assumed for their spatial distribution on any plane perpendicular to the propagation axis, simplifying the mathematical treatment. The theory is particularly useful for understanding beam behavior in simple geometries and serves as a foundation for more complex applications, such as pencil beam dose algorithms.

One can regard this theory as a way of propagating the phase-space distribution of the beam particles through a sequence of homogeneous mixed slabs. This is achieved by representing the beam particles in the phase space using the beam ellipse, which encloses the region where particles are most likely to be found. The area of this enclosed region is known as the root-mean-square emittance of the beam [Wied2015]. The geometric parameters of the beam ellipse, known as FE moments and indicated as $A_n(z) (n = 0,1,2)$, where z is the propagation axis, are propagated through the material by integrating the product of the scattering power $T(z)$ and polynomials up to second order along the beam path,

$$A_n(z) = \int_0^z (z-u)^n \, T(u) \, du \, . \tag{1}$$

Note that the FE moments are closely related to the well-known Twiss parameters [Wied2015] of the beam through simple formulas reported in the Appendix. For propagation through a sequence of mixed slabs, the cumulative FE moments are calculated in cascade using Eqs. (49-51) in [Gott2012].

The scattering power involved in this propagation of the FE moments is a function, which describes the rate of change with z of the variance of the MCS angle, projected onto each of the two transverse coordinates x and y. For instance, if one considers the coordinate x,

$$T(z) = \frac{d\langle\theta_x^2\rangle}{dz}. \tag{2}$$

This means that the FE moments in Eq. (1) need to be calculated for both the x and y projections to fully describe the transport of the beam. At the final propagation plane, the spatial and angular variances of the transmitted particle distribution are directly obtained from the values of the propagated FE moments using these formulas (and similar ones for y):

$$\langle x^2\rangle = A_2\,, \qquad \langle\theta_x^2\rangle = A_0\,, \tag{3}$$

while A_1 represents the covariance $\langle x\theta_x\rangle$ between the spatial and angular coordinates.

Various models were developed for the scattering power function [Gott2010]. Here, we choose to use the nonlocal differential approximation T_{dM} derived by Gottschalk using Molière's theory, defined as "differential Molière" scattering power, which has proven to be one of the most reliable models [Gott2010, Gott2012].

3. Transport of 63 and 71 MeV proton beams through the TOP-IMPLART scanning line

We consider a beam delivery line designed for scanning irradiations at the TOP-IMPLART accelerator in ENEA Frascati, aiming to estimate the transverse size of the propagated beam on the target plane. The delivery line in question was a first version of the definitive one. It slightly differs from the final version, currently under commissioning at the ENEA Frascati laboratories, only in the first air path length (~16.9 cm instead of ~13.0 cm). However, this small difference can be considered a minor perturbation to the results presented below, which nonetheless provide a realistic demonstration of particle transport, highlighting non-negligible discrepancies among the results obtained using the three calculation techniques employed.

Starting from the linac exit up to the target plane, the beam scanning line consisted of: a Ti window (thickness of 25 μm); a path in air (16.905 cm); an aluminized Mylar foil (22 μm); a He-filled chamber (170.790 cm); another aluminized Mylar foil (22 μm); and another path in air (60 cm). Each of the two aluminized Mylar foils was modeled as Mylar (20 μm) covered by an Al coating (2 μm). The total mass thickness of the line is 0.139 g/cm^2. The detailed design of this line is shown in Fig. 1. For two test cases with different mean energies, 63 and 71 MeV respectively, we compare the beam sizes on the target plane, estimated using three different approaches: SRIM simulation, FLUKA simulation, and FE theory. These beam sizes are calculated using the schematic setup shown in Fig. 2 for the particle transport problem, both for the aforementioned MC codes and the FE theory.

3.1 Beam characteristics on the source plane

Prior to calculating the beam transport, either using MC software or FE theory, a preliminary simulation of particle acceleration and propagation inside the accelerator modules was conducted using LINAC

software [Cran1994]. This simulation generated the phase-space coordinates of approximately 13,000 protons on the source plane shown in Fig. 2. For both the considered energies, these phase-space coordinates were processed using a Mathematica [Math2025] program to evaluate the energy spectra, the spatial distributions of particles and their phase-space diagrams on the source plane. During this process, particles with excessively peripheral phase-space coordinates were excluded from the analysis, retaining 95% of the original particles. The 63 MeV energy spectrum was fitted with a Gaussian function, while the slightly asymmetric shape of the 71 MeV energy spectrum suggested fitting it, also on the target plane, with an EMG function (Exponentially Modified Gaussian), which is defined as

$$\mathrm{EMG}(E) = \frac{\lambda}{2}\exp\left[-\lambda\left(\mu - E - \sigma^2\frac{\lambda}{2}\right)\right]\left[1 + \mathrm{erf}\left(\frac{\mu - E - \sigma^2\lambda}{\sqrt{2}\,\sigma}\right)\right], \tag{4}$$

where E is the energy variable, while μ, σ, and λ are fit parameters. Figures 3 and 4 illustrate the beam characteristics on the source plane for the 63 and 71 MeV cases, respectively, while Tabs. 1 and 2 list the parameter values resulting from the analysis. The differences among the parameter values obtained from the best fits and the covariance matrices is ascribable to the non-perfect Gaussian shape of the distributions.

3.2 Source plane phase-space processing

The two LINAC output files containing the phase-space coordinates for the 63 and 71 MeV cases were further processed using MATLAB [Matl2010] and Mathematica programs to write suitably formatted files for use as source input in SRIM and FLUKA, respectively. Another Mathematica program was coded to calculate the FE moments [Gott2010, Gott2012] from the phase-space coordinates, after excluding those particles with excessively peripheral coordinate values, retaining 95% of the original particles. Furthermore, using Mathematica to evaluate the covariance matrix of the LINAC output data, a further source input file was created exclusively for FLUKA. This file contained the coordinates of 500,000 particles sharing the same phase-space statistical distribution as the original, aiming to improve the accuracy of the FLUKA simulation.

We first present the results concerning the distributions of protons on the target plane obtained through MC simulations. As for the FE theory results, shown later on, they pertain the transport of the beam ellipse, from which the standard deviations of the Gaussian distributions of spatial and angular coordinates on the target plane are derived. The energy parameters of the transported beams are obtained by processing the outputs of the MC simulations and using the analytical formulas reported in [Nich2024], specifically Eqs. (12) and (13).

3.3 Monte Carlo simulations of 63 and 71 MeV beam propagation

The source files converted as specified above for being used as input in SRIM and FLUKA allowed running MC simulations of propagation in these two pieces of software along the beam delivery line schematized in Fig. 2. For the 63 MeV case, the resulting distributions on the target plane are shown in Figs. 5 and 6. The corresponding parameter values are listed in Tabs. 3 and 4. In FLUKA, another propagation simulation was run using, this time, the enlarged source input file containing 500,000 particles. The results of this simulation are reported in Fig. 7 and Tab. 5.

Similarly to the 63 MeV case, the source files obtained as explained in Sec. 3.2 were used as input in SRIM and FLUKA for the 71 MeV simulations of beam propagation along the delivery line schematized in Fig. 2. The resulting distributions on the target plane are shown in Figs. 8 and 9, with the

corresponding parameter values listed in Tabs. 6 and 7. The results of the additional FLUKA simulation run with an enlarged source input file containing 500,000 particles are reported in Fig. 10 and Tab. 8.

3.4. Fermi-Eyges calculation of 63 and 71 MeV beam propagation

Using FE theory, the beam ellipses in the phase space were propagated from the source plane to the target plane for the 63 and 71 MeV cases. The Twiss parameters obtained from the covariance matrices, listed in Tabs. 1 and 2, were utilized for this task.[1] Then, the FE moments at the source plane were calculated from these Twiss parameters using the conversion formulas reported in the Appendix. Regarding the propagation of the energy spectra, assumed to be Gaussian, it was performed by applying Eqs. (12) and (13) of [Nich2024] to the source-plane parameters E_0 and σ_E listed in Tab. 1, as well as to the parameters resulting from a Gaussian fit of the 71 MeV source spectrum, which are $E_0 = 71.05$ MeV and $\sigma_E = 192.2$ keV. The resulting values of the beam parameters on the target plane are reported in Tabs. 9 and 10.

3.5 Propagation of the 71 MeV beam up to the first aluminized Mylar window

As a further test, we examined the propagation at 71 MeV through the first section of the delivery line, specifically the 25-μm thick Ti window and the 16.905-cm long air path. This was done to check if differences between the SRIM and the FLUKA results start being present from the very beginning of the beam propagation. This is indeed the case, as evidenced by the plots in Figs. 11-12 and the values reported in Tabs. 11-12. (The EMG function was used to fit the energy spectra due to their slight asymmetry.) By comparing the values obtained by either the bivariate Gaussian fits or the covariance matrices, one sees that even along this reduced line, both the spatial and angular standard deviations derived from the SRIM simulations are smaller than the corresponding ones derived from the FLUKA simulations. As far as the values predicted by the FE theory, listed in Tab. 13, are concerned, they place themselves approximately halfway between those of the two MC software, with values closer to the FLUKA derived ones in the case of the angular parameters.

4. Test comparison with EBT3 measurement

A test comparing SRIM and FLUKA simulations to actual measurements of the beam size is useful for better understanding which of the two MC codes is more reliable. To this purpose, the proton-beam transverse spot of the TOP-IMPLART linac was recorded onto an EBT3 Gafchromic film [Ashl2025] placed at a distance of 252.3 cm from the exit Ti window. Propagation occurred entirely in the air up to the EBT3 film by removing the aluminized Mylar foils and not filling the space between them with helium (see Figs. 1 and 2).

Gafchromic films are routinely used in dosimetry for both medical and industrial applications to monitor and characterize particle beams, as well as to measure the total delivered dose. The EBT3 films consist of a 28 μm thick active layer, sandwiched between two 125 μm matte-polyester substrates, making them nearly tissue-equivalent. In this test, an EBT3 film was employed as a 2D radiation detector, offering high spatial resolution and a dynamic dose range spanning from 0.1 Gy to 20 Gy.

The EBT3 film was irradiated for 3 s with a dose rate of approximately 0.93 Gy/s, resulting in a total dose of approximately 2.8 Gy. It was then digitized using an Epson Expression 11000XL flatbed scanner in transmission mode, with no color correction applied, a resolution of 400 dpi, and a 24-bit color depth. The digitized image, converted to gray scale for subsequent analysis, is shown in Fig. 13. Transverse

[1] While the values shown in Tabs. 1 and 2 are rounded to the first significant digit of their uncertainties, the calculations were performed using the unrounded values.

profiles along the horizontal and vertical diameters of the circular region of interest were extracted using a Matlab script, based on the general calibration equation outlined in [Camp2017, Caso2019]. These profiles are shown in Fig. 14, along with the corresponding MC simulations performed with SRIM and FLUKA. The simulations used the phase-space distributions from Fig. 4 and Tab. 2 as input for the simulated in-air propagation from the source plane to the EBT3 position. Figure 14 also includes the Gaussian profiles obtained by calculating the beam propagation using the FE theory and the FE moments derived from the Twiss parameters shown in Tab. 2. The standard deviations of these profiles, along with those of the Gaussian fits of the measured and MC simulated profiles, are listed in Tab. 14.

The results of this test demonstrate the low reliability of the SRIM simulations regarding the propagation of the beam spot size. On the other hand, the profiles simulated in FLUKA, and even those calculated with the FE theory, are in quite good agreement with the measured ones. The latter are slightly wider, but we can attribute this to an imperfect match between the LINAC simulated phase-space characteristics at the source plane and the real ones.

5. Discussion and conclusions

Comparing the results reported in Tabs. 3-8, one notices that the beam spot size on the target plane obtained from the SRIM simulations is always significantly smaller than that obtained from the FLUKA simulations for both considered energies. This observation holds true whether considering the fit results or the covariance matrix ones, and whether taking into account the standard deviations obtained from the spatial coordinate distributions or from the phase-space diagrams. A similar difference is observed when considering the standard deviations of the angular coordinates. On the other hand, the energy spectra propagated with SRIM and with FLUKA agree to a very good degree.

We have not found any similar study in the literature comparing SRIM and FLUKA in the presence of delivery lines with mixed materials, and we have no immediate explanation for the observed differences. However, such a comparison, including other MC software, was recently reported for 158.6 MeV protons in [Andr2021], but it only covered scattering inside isolated single-element targets. In our case, we can hypothesize that the BCA utilized by SRIM is less accurate in presence of denser materials, where multiple contemporaneous interaction of the projectile with the material atoms become significant. This hypothesis is supported by our propagation test, reported in Sec. 3.5, limited to the initial section of the beam delivery line, where SRIM underestimates the angular width of the transmitted beam compared to FLUKA. This underestimation was also observed when simulating the propagation of ideal monochromatic pencil beams with energies 63 and 71 MeV in this initial section of the line (not reported in this Technical Report), thus excluding the possible influence of a specific starting phase-space distribution on the results. Moreover, the fact that FLUKA is a more comprehensive simulation software, accounting for many more physical processes than SRIM (whose most recent version is from 2013), along with its continuous development and validation by the scientific community, leads us to believe that the results obtained with FLUKA could be more reliable. This conclusion is supported by the experimental test reported in Sec. 4.

In all the examined cases, the results obtained with the FE theory, although approximate, have always been found to be quite close to the FLUKA simulations. More tests are planned to assess the reliability of the FE theory. Indeed, the availability of such a tool will enable us to perform quick evaluations of quantities such as the beam spot size and angular divergence at the target plane, which are useful for designing irradiation setups in the TOP-IMPLART facility.

Appendix

In this Appendix, we report the formulas that connect the FE moments with the Twiss parameters of the beam. The Twiss parameters (α, β, γ, ε) are commonly utilized to characterize the spatial and angular characteristics of a particle beam [Wied2015]. Leaving the demonstration to the reader, the formulas shown below can be easily derived by using the relationships existing between the parameters and the variances and covariance of the spatial and angular coordinates.

The formulas are

$$\alpha = -\frac{A_1}{\varepsilon}\,, \qquad \beta = \frac{A_2}{\varepsilon}\,, \qquad \gamma = \frac{A_0}{\varepsilon}\,, \qquad \varepsilon = \sqrt{B}\,, \tag{A.1}$$

with $B = A_0 A_2 - A_1^2$. The value of γ is often not reported, as it can be calculated from α and β using $\gamma = (1 + \alpha^2)/\beta$. The inverse formulas of Eq. (A.1) are

$$A_0 = \gamma\varepsilon, \qquad A_1 = -\alpha\varepsilon, \qquad A_2 = \beta\varepsilon, \qquad B = \varepsilon^2. \tag{A.2}$$

Acknowledgments

This research has been carried on within the TOP-IMPLART (Oncological Therapy with Protons – Intensity Modulated Proton Linear Accelerator for Radiotherapy) project funded by Regione Lazio, Italy.

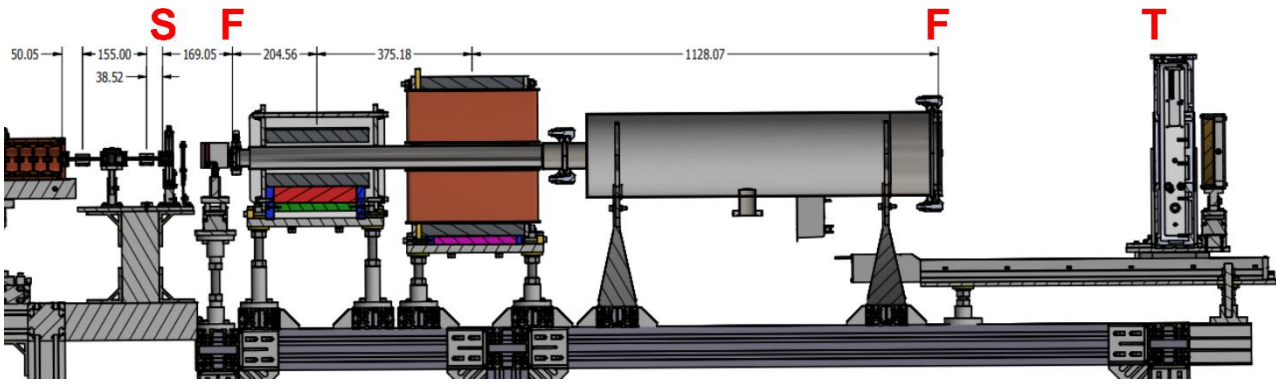

Figure 1. Design of the beam scanning line (first version) considered for the example evaluations of beam transport reported in Sec. 3. The letters at the top of the figure indicate the positions of the planes shown in Fig. 2, with the following meanings: S = source plane and attached Ti window, F = aluminized Mylar foils, T = target plane. The beam propagates from left to right. Measurements are in mm.

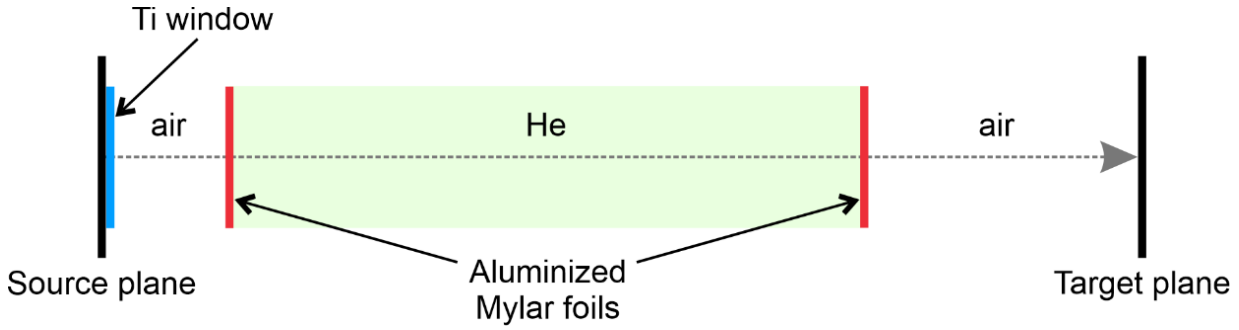

Figure 2. Schematic (not to scale) of the setup used for the example evaluations of proton beam transport, reported in Sec. 3, utilizing MC simulations in SRIM and FLUKA, and FE theory. The beam propagates from left to right.

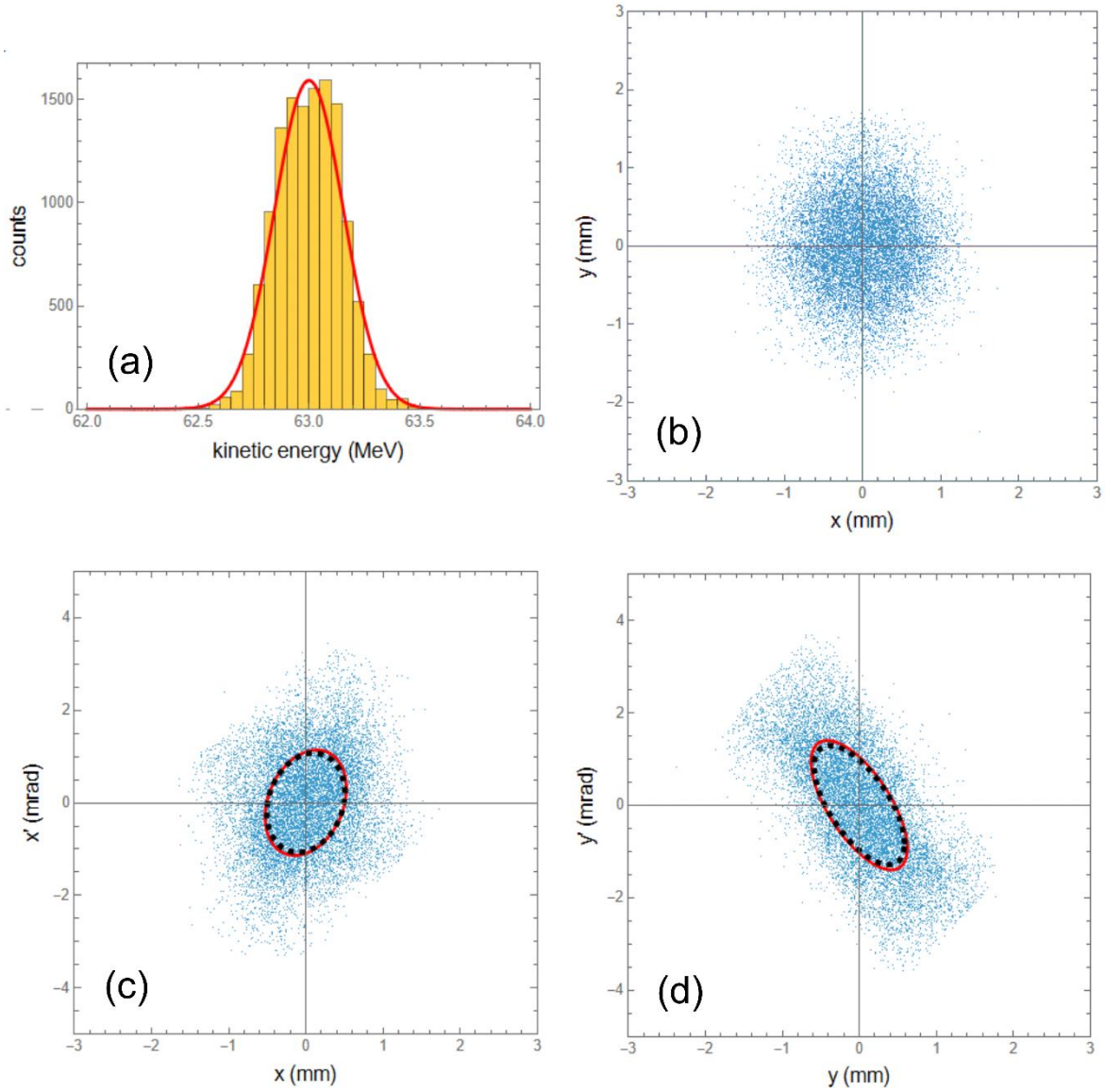

Figure 3. Source-plane characteristics of the 63 MeV proton beam obtained by processing the phase-space output data of a LINAC simulation: (a) energy spectrum (histogram) with its Gaussian fit (red line); (b) spatial coordinate distribution; (c) phase-space diagram for the x-projection; (d) phase-space diagram for the y-projection. The red and dotted black ellipses on these phase-space diagrams are contours that enclose about 68.3% of the total number of particles, obtained by best fitting the space-slope coordinates with a bivariate Gaussian function and directly from their covariance matrix, respectively.

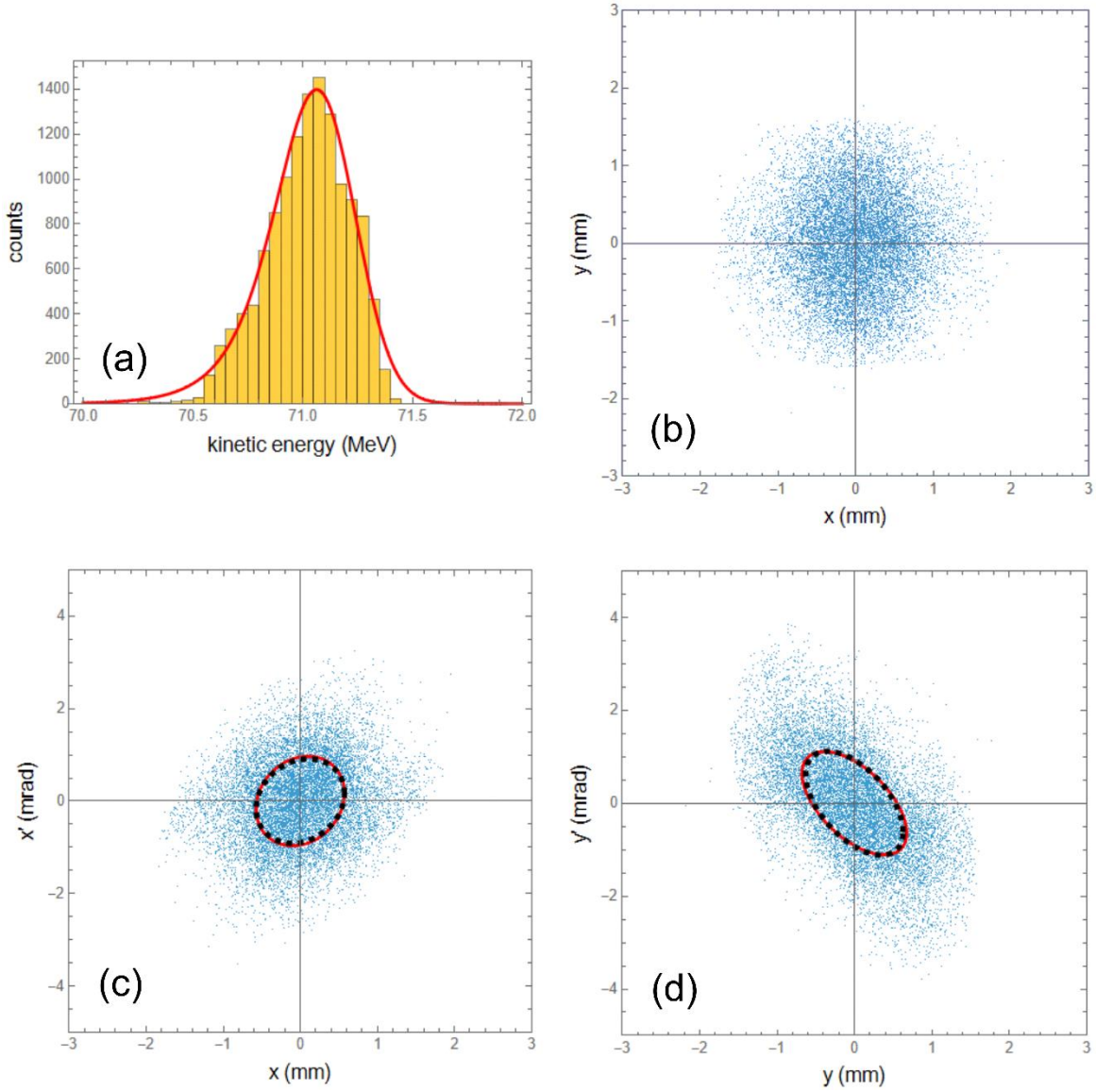

Figure 4. Source-plane characteristics of the 71 MeV proton beam obtained by processing the phase-space output data of a LINAC simulation: (a) energy spectrum (histogram) with its EMG fit (red line); (b) spatial coordinate distribution; (c) phase-space diagram for the x-projection; (d) phase-space diagram for the y-projection. The red and dotted black ellipses on these phase-space diagrams are contours that enclose about 68.3% of the total number of particles, obtained by best fitting the space-slope coordinates with a bivariate Gaussian function and directly from their covariance matrix, respectively.

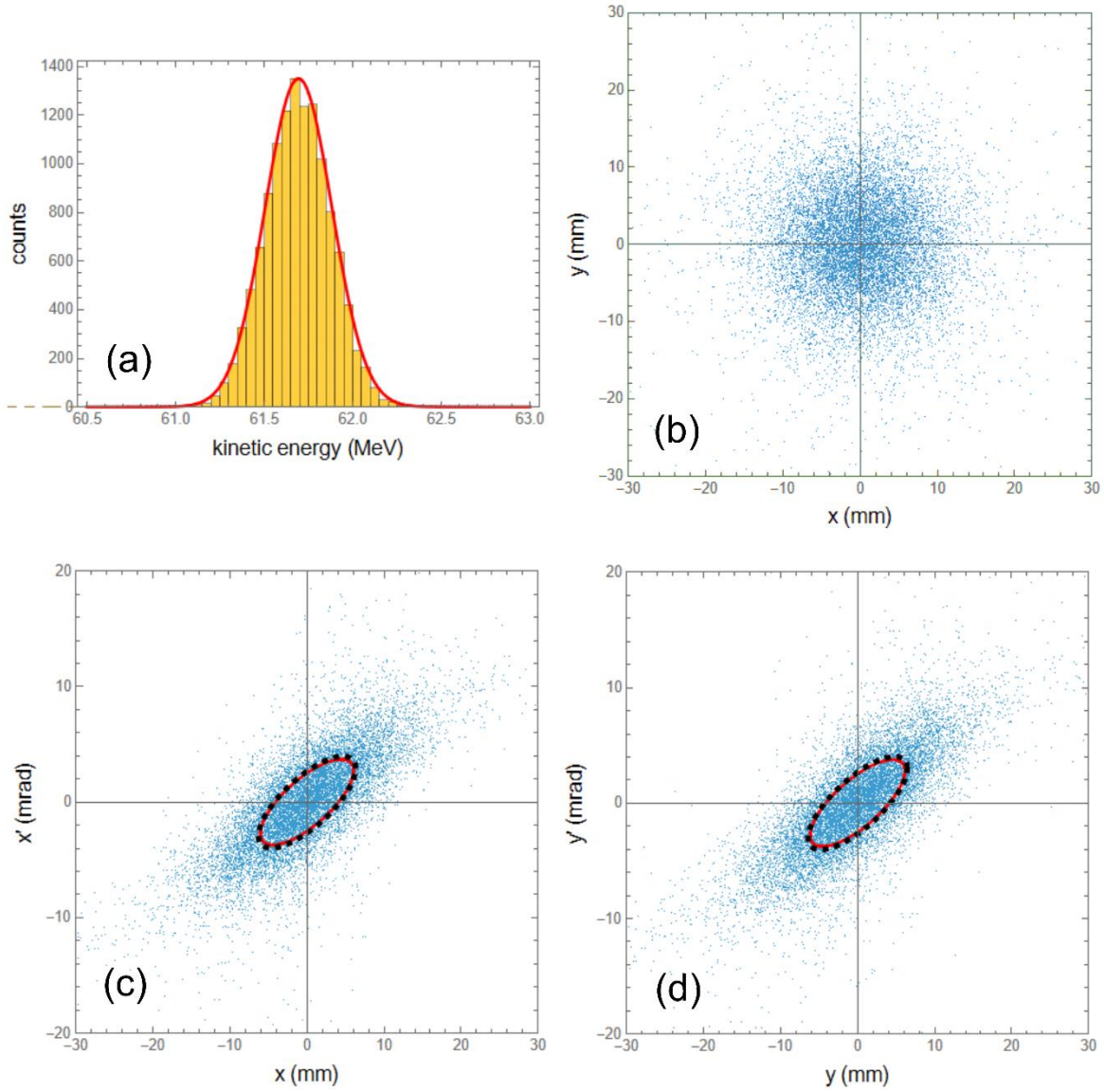

Figure 5. Target-plane characteristics of the 63 MeV proton beam obtained by processing the phase-space output data of a SRIM simulation: (a) energy spectrum (histogram) with its Gaussian fit (red line); (b) spatial coordinate distribution; (c) phase-space diagram for the x-projection; (d) phase-space diagram for the y-projection. The red and dotted black ellipses on these phase-space diagrams are contours that enclose about 68.3% of the total number of particles, obtained by best fitting the space-slope coordinates with a bivariate Gaussian function and directly from their covariance matrix, respectively.

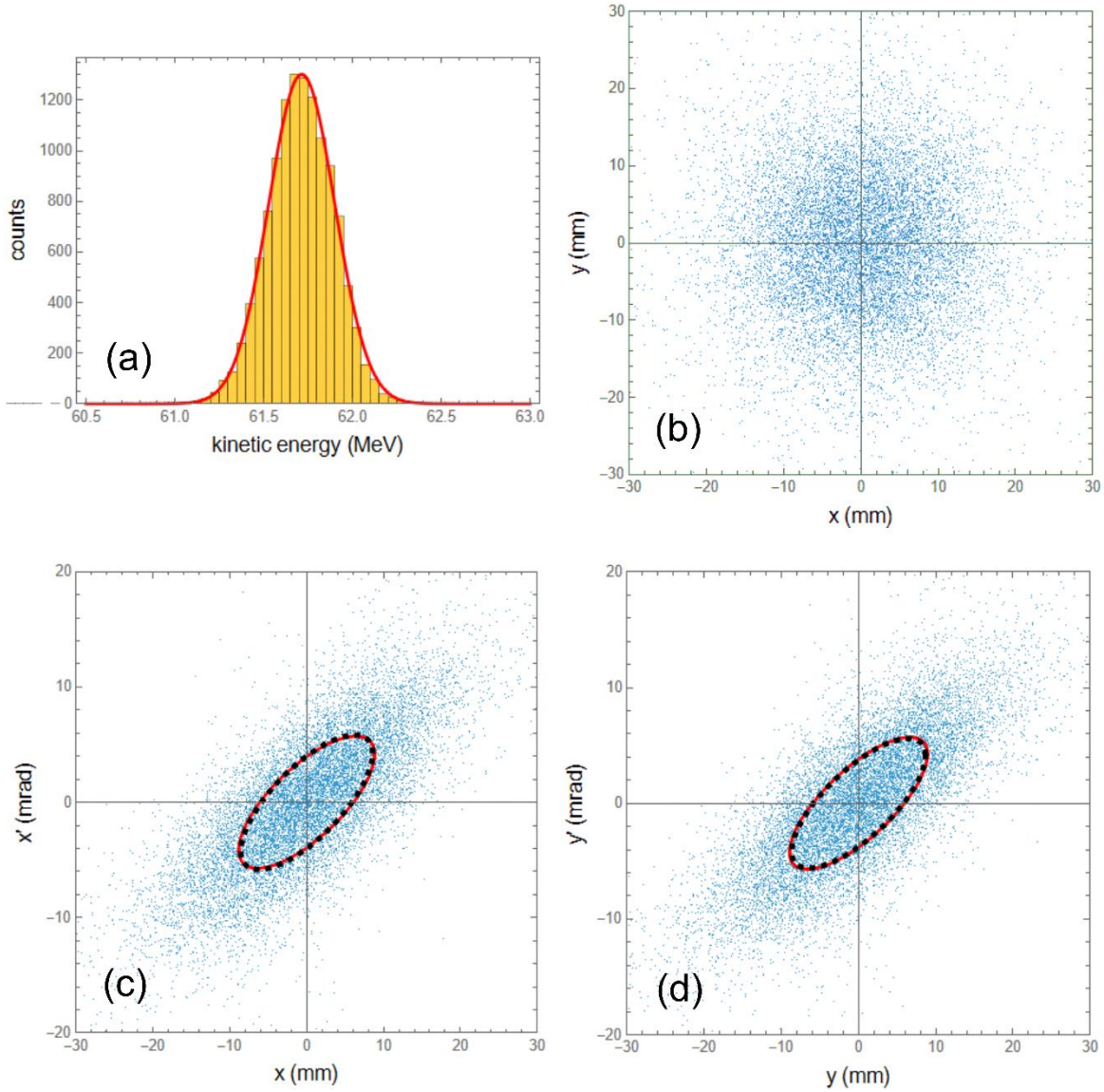

Figure 6. Target-plane characteristics of the 63 MeV proton beam obtained by processing the phase-space output data of a FLUKA simulation: (a) energy spectrum (histogram) with its Gaussian fit (red line); (b) spatial coordinate distribution; (c) phase-space diagram for the x-projection; (d) phase-space diagram for the y-projection. The red and dotted black ellipses on these phase-space diagrams are contours that enclose about 68.3% of the total number of particles, obtained by best fitting the space-slope coordinates with a bivariate Gaussian function and directly from their covariance matrix, respectively.

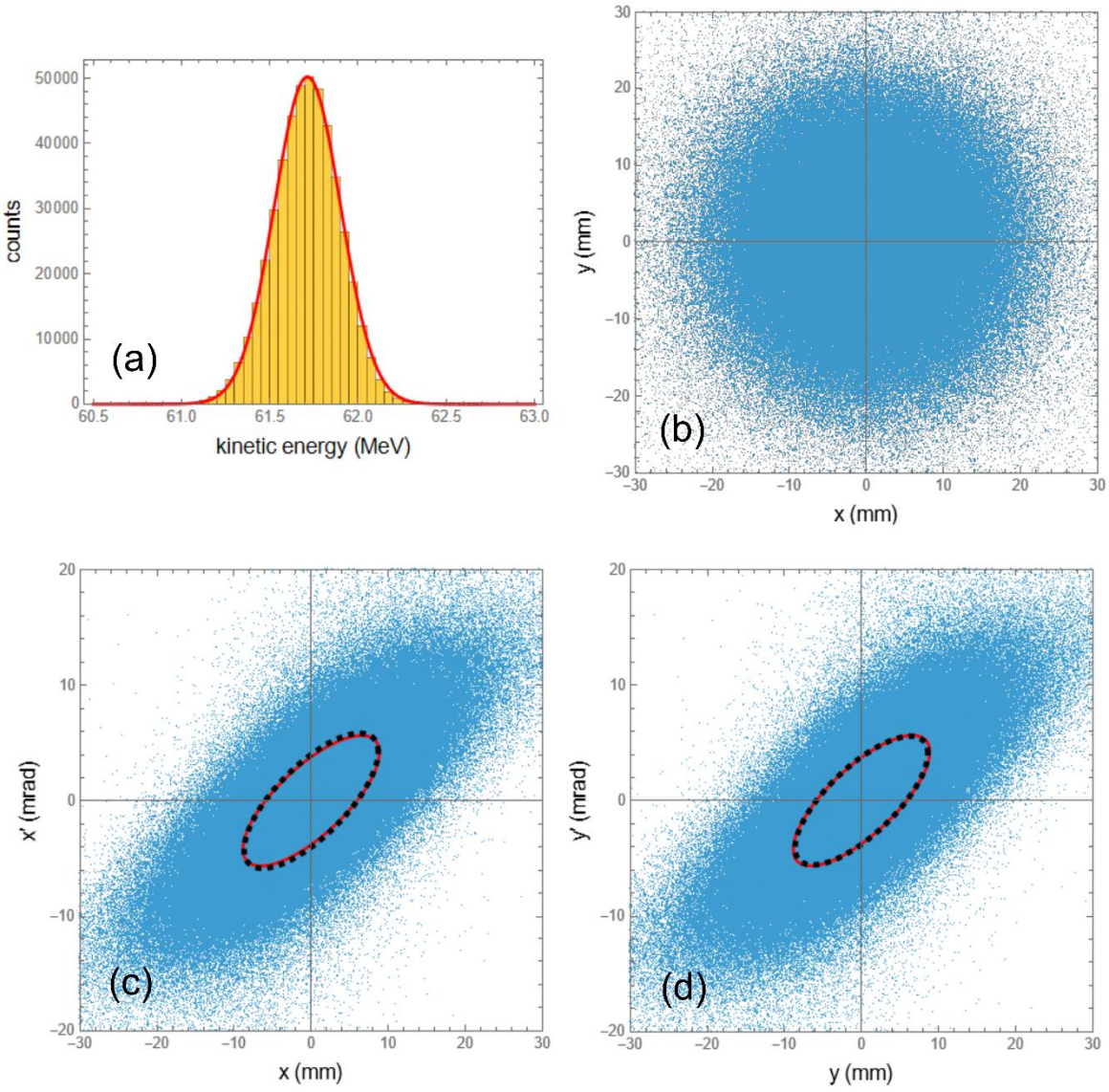

Figure 7. Target-plane characteristics of the 63 MeV proton beam obtained by processing the phase-space output data of a FLUKA simulation with an enlarged number of particles (500,000): (a) energy spectrum (histogram) with its Gaussian fit (red line); (b) spatial coordinate distribution; (c) phase-space diagram for the x-projection; (d) phase-space diagram for the y-projection. The red and dotted black ellipses on these phase-space diagrams are contours that enclose about 68.3% of the total number of particles, obtained by best fitting the space-slope coordinates with a bivariate Gaussian function and directly from their covariance matrix, respectively.

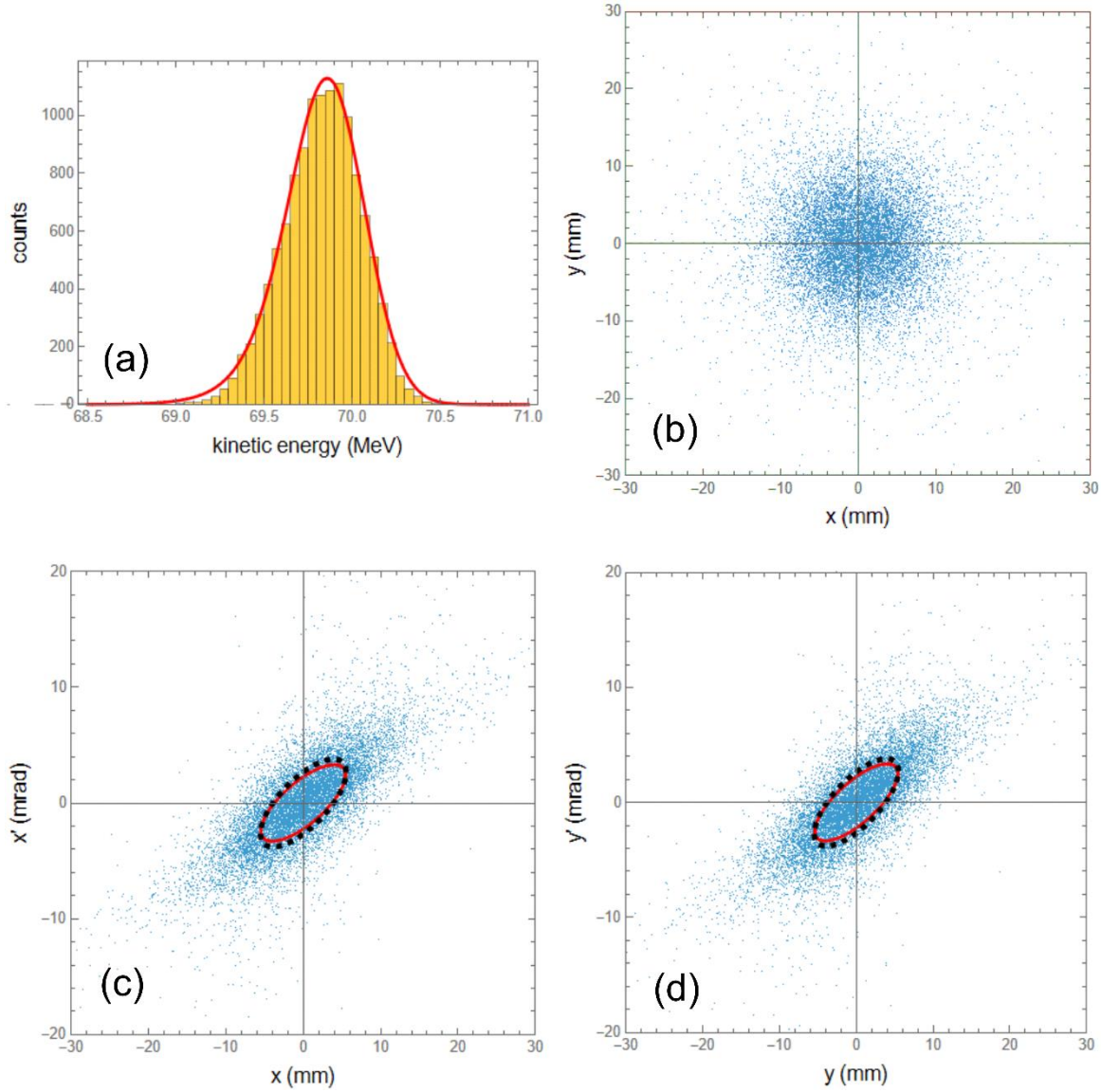

Figure 8. Target-plane characteristics of the 71 MeV proton beam obtained by processing the phase-space output data of a SRIM simulation: (a) energy spectrum (histogram) with its EMG fit (red line); (b) spatial coordinate distribution; (c) phase-space diagram for the x-projection; (d) phase-space diagram for the y-projection. The red and dotted black ellipses on these phase-space diagrams are contours that enclose about 68.3% of the total number of particles, obtained by best fitting the space-slope coordinates with a bivariate Gaussian function and directly from their covariance matrix, respectively.

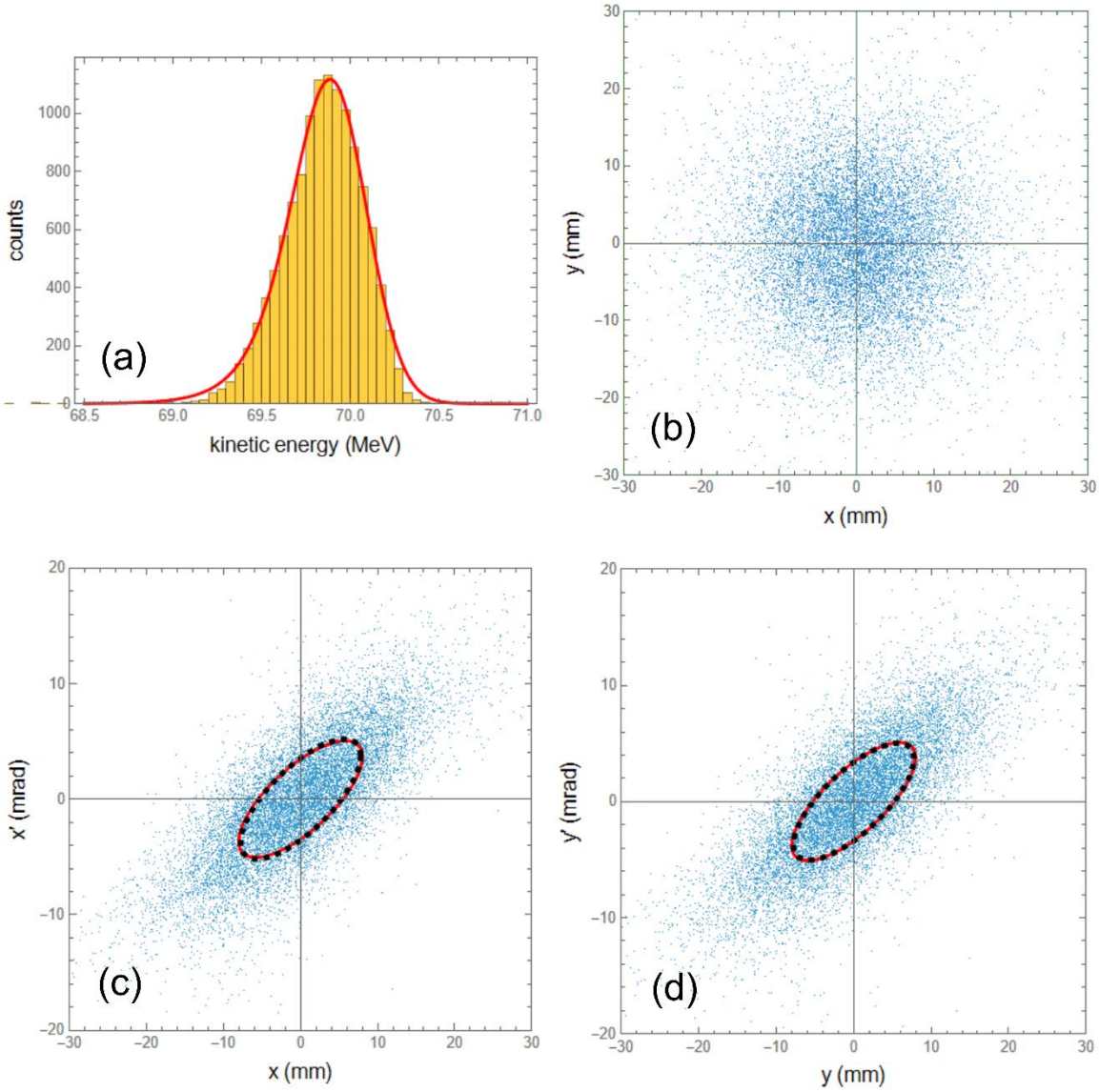

Figure 9. Target-plane characteristics of the 71 MeV proton beam obtained by processing the phase-space output data of a FLUKA simulation: (a) energy spectrum (histogram) with its EMG fit (red line); (b) spatial coordinate distribution; (c) phase-space diagram for the x-projection; (d) phase-space diagram for the y-projection. The red and dotted black ellipses on these phase-space diagrams are contours that enclose about 68.3% of the total number of particles, obtained by best fitting the space-slope coordinates with a bivariate Gaussian function and directly from their covariance matrix, respectively.

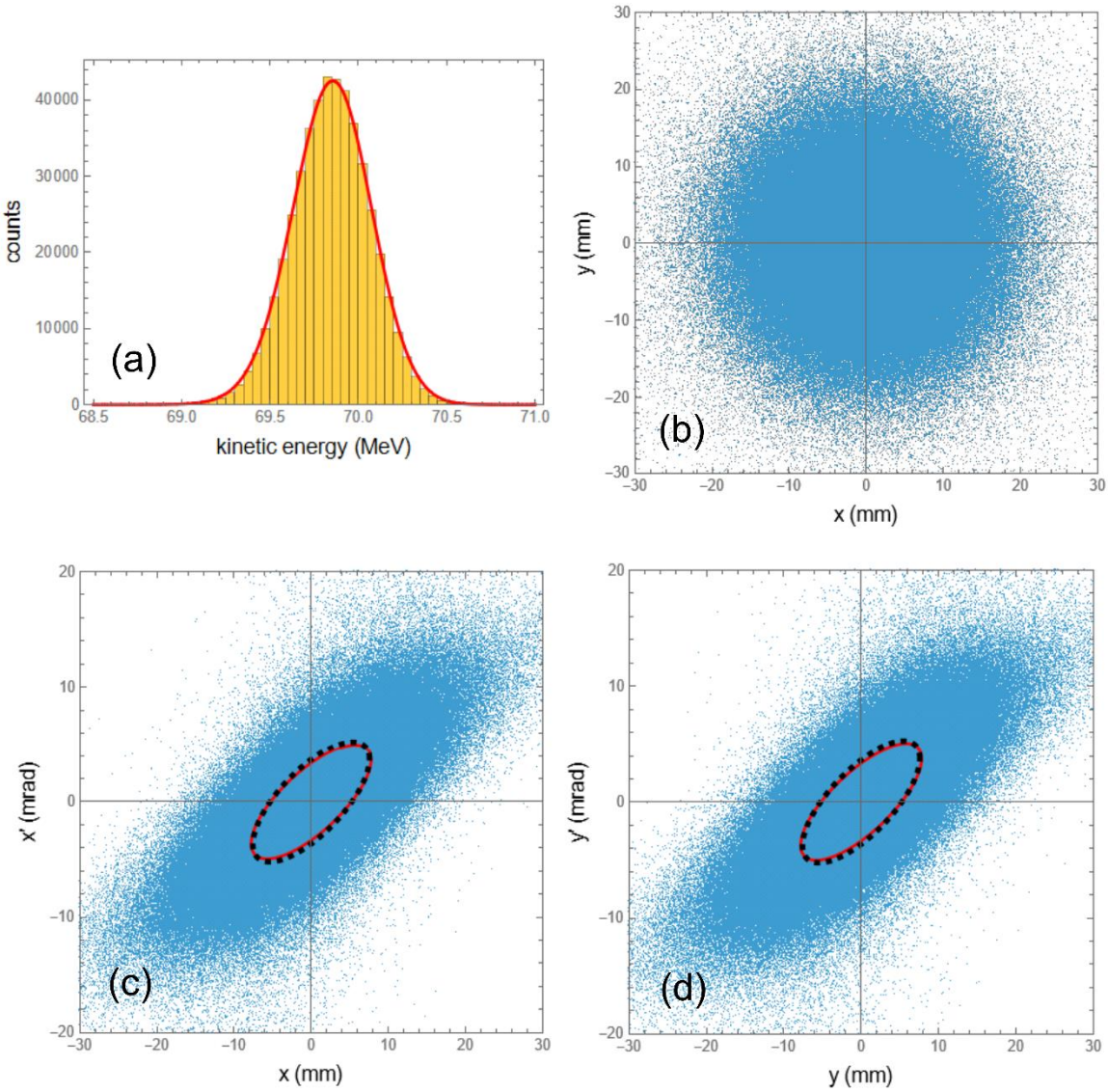

Figure 10. Target-plane characteristics of the 71 MeV proton beam obtained by processing the phase-space output data of a FLUKA simulation with an enlarged number of particles (500,000): (a) energy spectrum (histogram) with its EMG fit (red line); (b) spatial coordinate distribution; (c) phase-space diagram for the x-projection; (d) phase-space diagram for the y-projection. The red and dotted black ellipses on these phase-space diagrams are contours that enclose about 68.3% of the total number of particles, obtained by best fitting the space-slope coordinates with a bivariate Gaussian function and directly from their covariance matrix, respectively.

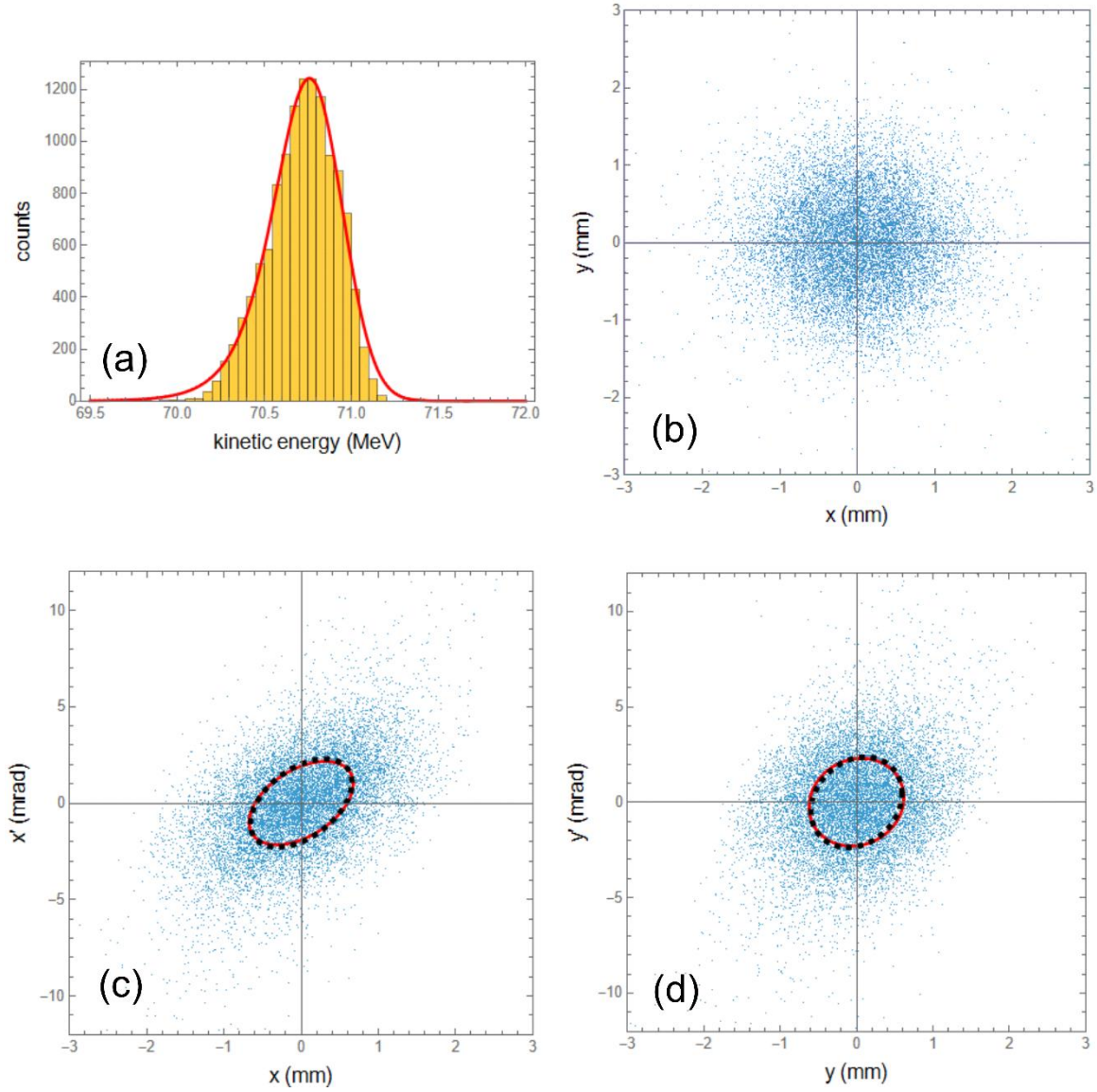

Figure 11. Characteristics of the 71 MeV proton beam propagated up to the aluminized Mylar foil, obtained by processing the phase-space output data of a SRIM simulation: (a) energy spectrum (histogram) with its EMG fit (red line); (b) spatial coordinate distribution; (c) phase-space diagram for the x-projection; (d) phase-space diagram for the y-projection. The red and dotted black ellipses on these phase-space diagrams are contours that enclose about 68.3% of the total number of particles, obtained by best fitting the space-slope coordinates with a bivariate Gaussian function and directly from their covariance matrix, respectively.

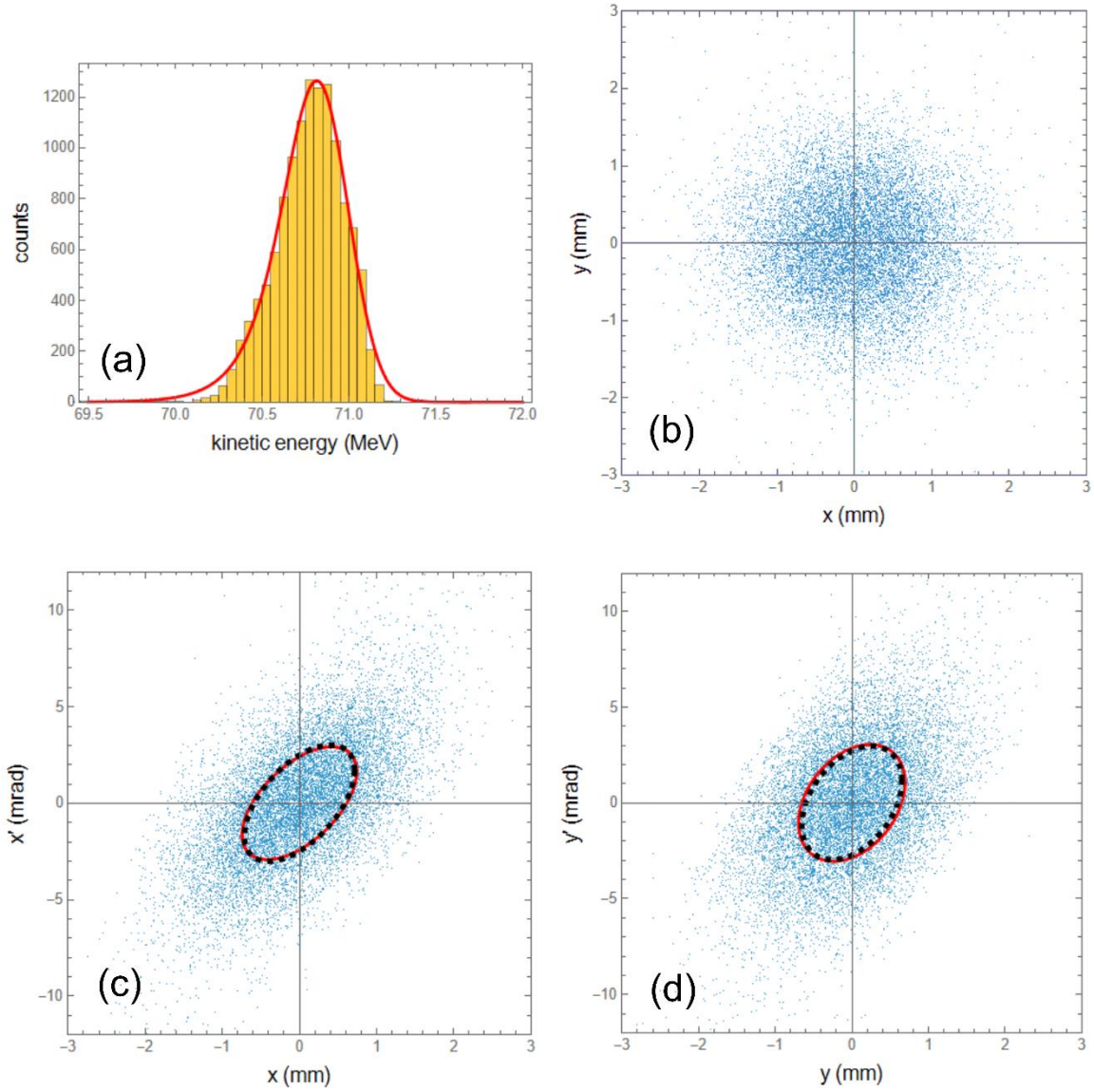

Figure 12. Characteristics of the 71 MeV proton beam propagated up to the aluminized Mylar foil, obtained by processing the phase-space output data of a FLUKA simulation: (a) energy spectrum (histogram) with its EMG fit (red line); (b) spatial coordinate distribution; (c) phase-space diagram for the x-projection; (d) phase-space diagram for the y-projection. The red and dotted black ellipses on these phase-space diagrams are contours that enclose about 68.3% of the total number of particles, obtained by best fitting the space-slope coordinates with a bivariate Gaussian function and directly from their covariance matrix, respectively.

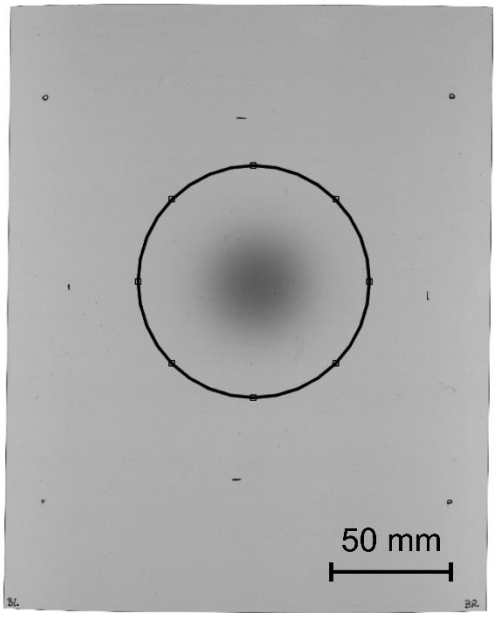

Figure 13. Digitized image of the EBT3 Gafchromic film irradiated with the 71 MeV TOP-IMPLART proton beam at a distance of 252.3 cm from the linac-exit Ti window. The circumference encloses the region of interest considered for the analysis.

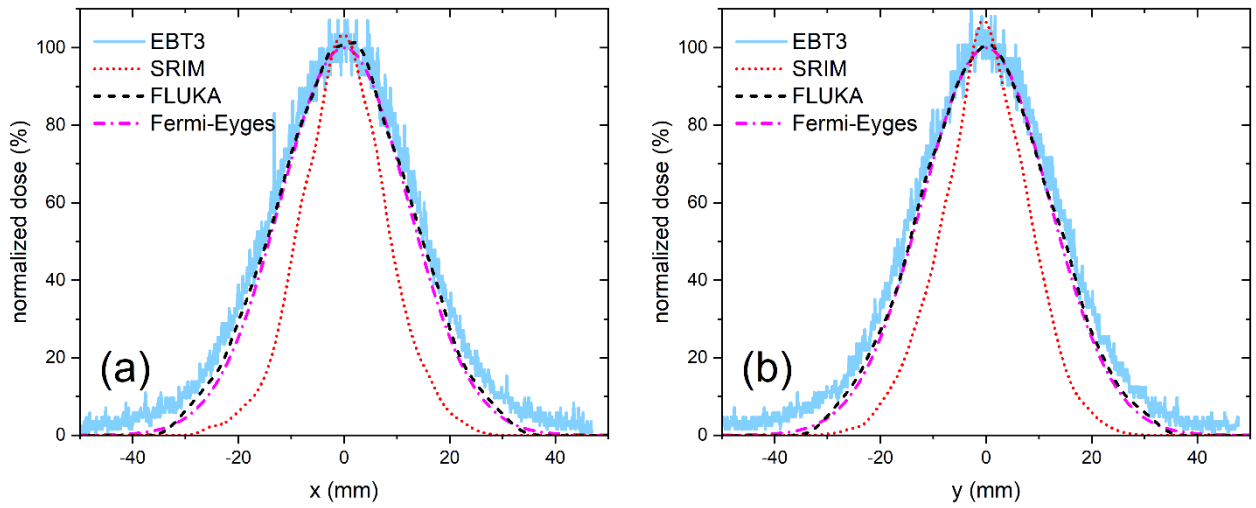

Figure 14. Measured (EBT3) and simulated (SRIM and FLUKA) dose profiles along the (a) x-axis and (b) y-axis resulting from the TOP-IMPLART 71 MeV proton-beam irradiation at a distance of 252.3 cm from the linac exit. The EBT3 profiles were extracted from the digitized image in Fig. 13 (b) along the horizontal and vertical diameters of the circular region of interest, each having a thickness of 1 pixel, corresponding to 63.5 μm. FE-calculated beam profiles (normalized to 100% dose) are also shown. See the text for more details.

Parameter	Value from best fit	Value from covariance matrix
E_0 (MeV)	63.001 ± 0.003	–
σ_E (keV)	155 ± 3	–
σ_x (mm)	0.556 ± 0.002	0.505 ± 0.006
σ_y (mm)	0.617 ± 0.003	0.587 ± 0.007
$\langle x^2 \rangle^{1/2}$ (mm)	0.53 ± 0.04	0.505 ± 0.006
$\langle \theta_x^2 \rangle^{1/2}$ (mrad)	1.14 ± 0.09	1.07 ± 0.01
$\langle x\theta_x \rangle$ (mm mrad)	0.162 ± 0.002	0.109 ± 0.001
$\langle y^2 \rangle^{1/2}$ (mm)	0.63 ± 0.06	0.587 ± 0.007
$\langle \theta_y^2 \rangle^{1/2}$ (mrad)	1.4 ± 0.1	1.29 ± 0.02
$\langle y\theta_y \rangle$ (mm mrad)	-0.584 ± 0.006	-0.492 ± 0.006
α_x	-0.279 ± 0.003	-0.205 ± 0.003
β_x (mm/mrad)	0.480 ± 0.003	0.481 ± 0.006
ε_x (mm mrad)	0.580 ± 0.003	0.530 ± 0.007
α_y	0.89 ± 0.02	0.86 ± 0.01
β_y (mm/mrad)	0.60 ± 0.01	0.601 ± 0.007
ε_y (mm mrad)	0.65 ± 0.01	0.573 ± 0.007

Table 1. Parameters of the 63 MeV proton beam at the source plane (see Fig. 3). From top to bottom: mean value E_0 and standard deviation σ_E of the energy spectrum; standard deviations σ_x and σ_y of the spatial coordinate distribution; standard deviations $\langle x^2 \rangle^{1/2}$ and $\langle \theta_x^2 \rangle^{1/2}$, and covariance $\langle x\theta_x \rangle$, of the phase-space diagram for the x-projection; standard deviations $\langle y^2 \rangle^{1/2}$ and $\langle \theta_y^2 \rangle^{1/2}$, and covariance $\langle y\theta_y \rangle$, of the phase-space diagram for the y-projection; Twiss parameters α_x, β_x, and ε_x for the x-projection; Twiss parameters α_y, β_y, and ε_y for the y-projection. Uncertainties are evaluated at the 95% confidence level.

Parameter	Value from best fit	Value from covariance matrix
μ (MeV)	71.170 ± 0.002	–
σ (keV)	152 ± 1	–
λ (MeV^{-1})	6.6 ± 0.1	–
σ_x (mm)	0.588 ± 0.002	0.573 ± 0.007
σ_y (mm)	0.700 ± 0.003	0.630 ± 0.008
$\langle x^2 \rangle^{1/2}$ (mm)	0.57 ± 0.04	0.573 ± 0.007
$\langle \theta_x^2 \rangle^{1/2}$ (mrad)	0.97 ± 0.07	0.91 ± 0.01
$\langle x\theta_x \rangle$ (mm mrad)	0.098 ± 0.01	0.096 ± 0.01
$\langle y^2 \rangle^{1/2}$ (mm)	0.68 ± 0.06	0.630 ± 0.008
$\langle \theta_y^2 \rangle^{1/2}$ (mrad)	1.11 ± 0.09	1.12 ± 0.01
$\langle y\theta_y \rangle$ (mm mrad)	-0.434 ± 0.003	-0.389 ± 0.005
α_x	-0.178 ± 0.002	-0.186 ± 0.002
β_x (mm/mrad)	0.602 ± 0.004	0.640 ± 0.008
ε_x (mm mrad)	0.549 ± 0.002	0.514 ± 0.006
α_y	0.703 ± 0.008	0.662 ± 0.008
β_y (mm/mrad)	0.743 ± 0.008	0.676 ± 0.008
ε_y (mm mrad)	0.617 ± 0.005	0.588 ± 0.007

Table 2. Parameters of the 71 MeV proton beam at the source plane (see Fig. 4). From top to bottom: parameters μ, σ, and λ of the energy spectrum (EMG fit); standard deviations σ_x and σ_y of the spatial coordinate distribution; standard deviations $\langle x^2 \rangle^{1/2}$ and $\langle \theta_x^2 \rangle^{1/2}$, and covariance $\langle x\theta_x \rangle$, of the phase-space diagram for the x-projection; standard deviations $\langle y^2 \rangle^{1/2}$ and $\langle \theta_y^2 \rangle^{1/2}$, and covariance $\langle y\theta_y \rangle$, of the phase-space diagram for the y-projection; Twiss parameters α_x, β_x, and ε_x for the x-projection; Twiss parameters α_y, β_y, and ε_y for the y-projection. Uncertainties are evaluated at the 95% confidence level.

Parameter	Value from best fit	Value from covariance matrix
E_0 (MeV)	61.6940 ± 0.0006	–
σ_E (keV)	188.7 ± 0.6	–
σ_x (mm)	5.92 ± 0.02	6.31 ± 0.08
σ_y (mm)	6.05 ± 0.02	6.45 ± 0.08
$\langle x^2 \rangle^{1/2}$ (mm)	6.1 ± 0.5	6.31 ± 0.08
$\langle \theta_x^2 \rangle^{1/2}$ (mrad)	3.7 ± 0.3	3.96 ± 0.05
$\langle x\theta_x \rangle$ (mm mrad)	16.6 ± 0.1	18.4 ± 0.2
$\langle y^2 \rangle^{1/2}$ (mm)	6.2 ± 0.5	6.45 ± 0.08
$\langle \theta_y^2 \rangle^{1/2}$ (mrad)	3.8 ± 0.3	4.03 ± 0.05
$\langle y\theta_y \rangle$ (mm mrad)	17.3 ± 0.1	19.5 ± 0.2
α_x	-1.08 ± 0.02	-1.09 ± 0.01
β_x (mm/mrad)	2.41 ± 0.03	2.35 ± 0.03
ε_x (mm mrad)	15.3 ± 0.2	16.9 ± 0.2
α_y	-1.11 ± 0.02	-1.13 ± 0.01
β_y (mm/mrad)	2.44 ± 0.03	2.41 ± 0.03
ε_y (mm mrad)	15.6 ± 0.02	17.2 ± 0.02

Table 3. Parameters of the 63 MeV proton beam at the target plane obtained by processing the SRIM simulation of Fig. 5. From top to bottom: mean value E_0 and standard deviation σ_E of the energy spectrum; standard deviations σ_x and σ_y of the spatial coordinate distribution; standard deviations $\langle x^2 \rangle^{1/2}$ and $\langle \theta_x^2 \rangle^{1/2}$, and covariance $\langle x\theta_x \rangle$, of the phase-space diagram for the x-projection; standard deviations $\langle y^2 \rangle^{1/2}$ and $\langle \theta_y^2 \rangle^{1/2}$, and covariance $\langle y\theta_y \rangle$, of the phase-space diagram for the y-projection; Twiss parameters α_x, β_x, and ε_x for the x-projection; Twiss parameters α_y, β_y, and ε_y for the y-projection. Uncertainties are evaluated at the 95% confidence level.

Parameter	Value from best fit	Value from covariance matrix
E_0 (MeV)	61.714 ± 0.003	–
σ_E (keV)	186 ± 3	–
σ_x (mm)	8.76 ± 0.04	8.6 ± 0.1
σ_y (mm)	8.74 ± 0.04	8.7 ± 0.1
$\langle x^2 \rangle^{1/2}$ (mm)	8.8 ± 0.2	8.6 ± 0.1
$\langle \theta_x^2 \rangle^{1/2}$ (mrad)	5.7 ± 0.2	5.83 ± 0.07
$\langle x\theta_x \rangle$ (mm mrad)	36.75 ± 0.03	36.3 ± 0.5
$\langle y^2 \rangle^{1/2}$ (mm)	9.0 ± 0.3	8.7 ± 0.1
$\langle \theta_y^2 \rangle^{1/2}$ (mrad)	5.7 ± 0.2	5.59 ± 0.07
$\langle y\theta_y \rangle$ (mm mrad)	38.12 ± 0.04	35.9 ± 0.5
α_x	-1.052 ± 0.002	-1.06 ± 0.01
β_x (mm/mrad)	2.241 ± 0.004	2.14 ± 0.03
ε_x (mm mrad)	34.94 ± 0.05	34.4 ± 0.4
α_y	-1.119 ± 0.002	-1.10 ± 0.01
β_y (mm/mrad)	2.353 ± 0.005	2.30 ± 0.03
ε_y (mm mrad)	34.07 ± 0.07	32.6 ± 0.4

Table 4. Parameters of the 63 MeV proton beam at the target plane obtained by processing the FLUKA simulation of Fig. 6. From top to bottom: mean value E_0 and standard deviation σ_E of the energy spectrum; standard deviations σ_x and σ_y of the spatial coordinate distribution; standard deviations $\langle x^2 \rangle^{1/2}$ and $\langle \theta_x^2 \rangle^{1/2}$, and covariance $\langle x\theta_x \rangle$, of the phase-space diagram for the x-projection; standard deviations $\langle y^2 \rangle^{1/2}$ and $\langle \theta_y^2 \rangle^{1/2}$, and covariance $\langle y\theta_y \rangle$, of the phase-space diagram for the y-projection; Twiss parameters α_x, β_x, and ε_x for the x-projection; Twiss parameters α_y, β_y, and ε_y for the y-projection. Uncertainties are evaluated at the 95% confidence level.

Parameter	Value from best fit	Value from covariance matrix
E_0 (MeV)	61.7139 ± 0.0006	–
σ_E (keV)	187.6 ± 0.6	–
σ_x (mm)	8.78 ± 0.02	8.70 ± 0.02
σ_y (mm)	8.71 ± 0.02	8.62 ± 0.02
$\langle x^2 \rangle^{1/2}$ (mm)	8.8 ± 0.2	8.70 ± 0.02
$\langle \theta_x^2 \rangle^{1/2}$ (mrad)	5.6 ± 0.1	5.84 ± 0.01
$\langle x\theta_x \rangle$ (mm mrad)	36.90 ± 0.02	36.90 ± 0.07
$\langle y^2 \rangle^{1/2}$ (mm)	8.9 ± 0.2	8.62 ± 0.02
$\langle \theta_y^2 \rangle^{1/2}$ (mrad)	5.6 ± 0.1	5.57 ± 0.01
$\langle y\theta_y \rangle$ (mm mrad)	37.37 ± 0.02	35.15 ± 0.07
α_x	-1.098 ± 0.001	-1.055 ± 0.002
β_x (mm/mrad)	2.329 ± 0.003	2.164 ± 0.004
ε_x (mm mrad)	33.62 ± 0.04	34.99 ± 0.07
α_y	-1.127 ± 0.001	-1.077 ± 0.002
β_y (mm/mrad)	2.364 ± 0.003	2.276 ± 0.005
ε_y (mm mrad)	33.15 ± 0.04	32.63 ± 0.07

Table 5. Parameters of the 63 MeV proton beam at the target plane obtained by processing the FLUKA simulation of Fig. 7. From top to bottom: mean value E_0 and standard deviation σ_E of the energy spectrum; standard deviations σ_x and σ_y of the spatial coordinate distribution; standard deviations $\langle x^2 \rangle^{1/2}$ and $\langle \theta_x^2 \rangle^{1/2}$, and covariance $\langle x\theta_x \rangle$, of the phase-space diagram for the x-projection; standard deviations $\langle y^2 \rangle^{1/2}$ and $\langle \theta_y^2 \rangle^{1/2}$, and covariance $\langle y\theta_y \rangle$, of the phase-space diagram for the y-projection; Twiss parameters α_x, β_x, and ε_x for the x-projection; Twiss parameters α_y, β_y, and ε_y for the y-projection. Uncertainties are evaluated at the 95% confidence level.

Parameter	Value from best fit	Value from covariance matrix
μ (MeV)	69.969 ± 0.001	–
σ (keV)	190.1 ± 0.7	–
λ (MeV^{-1})	7.02 ± 0.08	–
σ_x (mm)	5.43 ± 0.01	5.55 ± 0.07
σ_y (mm)	5.35 ± 0.01	5.49 ± 0.07
$\langle x^2 \rangle^{1/2}$ (mm)	5.5 ± 0.4	5.55 ± 0.07
$\langle \theta_x^2 \rangle^{1/2}$ (mrad)	3.3 ± 0.3	3.78 ± 0.05
$\langle x\theta_x \rangle$ (mm mrad)	13.35 ± 0.08	14.8 ± 0.2
$\langle y^2 \rangle^{1/2}$ (mm)	5.4 ± 0.5	5.49 ± 0.07
$\langle \theta_y^2 \rangle^{1/2}$ (mrad)	3.4 ± 0.3	3.80 ± 0.05
$\langle y\theta_y \rangle$ (mm mrad)	13.7 ± 0.1	14.9 ± 0.2
α_x	-1.08 ± 0.01	-0.99 ± 0.01
β_x (mm/mrad)	2.44 ± 0.03	2.07 ± 0.03
ε_x (mm mrad)	12.4 ± 0.1	14.9 ± 0.2
α_y	-1.13 ± 0.02	-1.02 ± 0.01
β_y (mm/mrad)	2.43 ± 0.04	2.06 ± 0.03
ε_y (mm mrad)	12.1 ± 0.02	14.6 ± 0.02

Table 6. Parameters of the 71 MeV proton beam at the target plane obtained by processing the SRIM simulation of Fig. 8. From top to bottom: parameters μ, σ, and λ of the energy spectrum (EMG fit); standard deviations σ_x and σ_y of the spatial coordinate distribution; standard deviations $\langle x^2 \rangle^{1/2}$ and $\langle \theta_x^2 \rangle^{1/2}$, and covariance $\langle x\theta_x \rangle$, of the phase-space diagram for the x-projection; standard deviations $\langle y^2 \rangle^{1/2}$ and $\langle \theta_y^2 \rangle^{1/2}$, and covariance $\langle y\theta_y \rangle$, of the phase-space diagram for the y-projection; Twiss parameters α_x, β_x, and ε_x for the x-projection; Twiss parameters α_y, β_y, and ε_y for the y-projection. Uncertainties are evaluated at the 95% confidence level.

Parameter	Value from best fit	Value from covariance matrix
μ (MeV)	70.002 ± 0.001	–
σ (keV)	180.5 ± 0.8	–
λ (MeV^{-1})	6.31 ± 0.07	–
σ_x (mm)	7.90 ± 0.04	7.8 ± 0.1
σ_y (mm)	7.84 ± 0.04	7.8 ± 0.1
$\langle x^2 \rangle^{1/2}$ (mm)	8.0 ± 0.2	7.8 ± 0.1
$\langle \theta_x^2 \rangle^{1/2}$ (mrad)	5.1 ± 0.2	5.17 ± 0.07
$\langle x\theta_x \rangle$ (mm mrad)	29.59 ± 0.03	29.3 ± 0.4
$\langle y^2 \rangle^{1/2}$ (mm)	8.0 ± 0.3	7.8 ± 0.1
$\langle \theta_y^2 \rangle^{1/2}$ (mrad)	5.1 ± 0.2	5.02 ± 0.06
$\langle y\theta_y \rangle$ (mm mrad)	30.36 ± 0.03	28.7 ± 0.4
α_x	-1.060 ± 0.002	-1.06 ± 0.01
β_x (mm/mrad)	2.319 ± 0.005	2.19 ± 0.03
ε_x (mm mrad)	27.92 ± 0.05	27.6 ± 0.4
α_y	-1.122 ± 0.003	-1.09 ± 0.01
β_y (mm/mrad)	2.353 ± 0.006	2.29 ± 0.03
ε_y (mm mrad)	27.07 ± 0.06	26.3 ± 0.3

Table 7. Parameters of the 71 MeV proton beam at the target plane obtained by processing the FLUKA simulation of Fig. 9. From top to bottom: parameters μ, σ, and λ of the energy spectrum (EMG fit); standard deviations σ_x and σ_y of the spatial coordinate distribution; standard deviations $\langle x^2 \rangle^{1/2}$ and $\langle \theta_x^2 \rangle^{1/2}$, and covariance $\langle x\theta_x \rangle$, of the phase-space diagram for the x-projection; standard deviations $\langle y^2 \rangle^{1/2}$ and $\langle \theta_y^2 \rangle^{1/2}$, and covariance $\langle y\theta_y \rangle$, of the phase-space diagram for the y-projection; Twiss parameters α_x, β_x, and ε_x for the x-projection; Twiss parameters α_y, β_y, and ε_y for the y-projection. Uncertainties are evaluated at the 95% confidence level.

Parameter	Value from best fit	Value from covariance matrix
μ (MeV)	69.9276 ± 0.0004	–
σ (keV)	210.5 ± 0.2	–
λ (MeV^{-1})	12.49 ± 0.08	–
σ_x (mm)	7.71 ± 0.02	7.56 ± 0.02
σ_y (mm)	7.75 ± 0.02	7.59 ± 0.02
$\langle x^2 \rangle^{1/2}$ (mm)	7.8 ± 0.2	7.56 ± 0.02
$\langle \theta_x^2 \rangle^{1/2}$ (mrad)	5.0 ± 0.1	5.21 ± 0.01
$\langle x\theta_x \rangle$ (mm mrad)	28.41 ± 0.02	28.10 ± 0.06
$\langle y^2 \rangle^{1/2}$ (mm)	7.8 ± 0.2	7.59 ± 0.02
$\langle \theta_y^2 \rangle^{1/2}$ (mrad)	5.0 ± 0.1	5.24 ± 0.01
$\langle y\theta_y \rangle$ (mm mrad)	29.24 ± 0.02	28.65 ± 0.06
α_x	-1.088 ± 0.001	-1.015 ± 0.002
β_x (mm/mrad)	2.316 ± 0.003	2.067 ± 0.004
ε_x (mm mrad)	26.11 ± 0.03	27.68 ± 0.06
α_y	-1.115 ± 0.002	-1.037 ± 0.002
β_y (mm/mrad)	2.327 ± 0.003	2.085 ± 0.004
ε_y (mm mrad)	26.22 ± 0.03	27.62 ± 0.06

Table 8. Parameters of the 71 MeV proton beam at the target plane obtained by processing the FLUKA simulation of Fig. 10. From top to bottom: : parameters μ, σ, and λ of the energy spectrum (EMG fit); standard deviations σ_x and σ_y of the spatial coordinate distribution; standard deviations $\langle x^2 \rangle^{1/2}$ and $\langle \theta_x^2 \rangle^{1/2}$, and covariance $\langle x\theta_x \rangle$, of the phase-space diagram for the x-projection; standard deviations $\langle y^2 \rangle^{1/2}$ and $\langle \theta_y^2 \rangle^{1/2}$, and covariance $\langle y\theta_y \rangle$, of the phase-space diagram for the y-projection; Twiss parameters α_x, β_x, and ε_x for the x-projection; Twiss parameters α_y, β_y, and ε_y for the y-projection. Uncertainties are evaluated at the 95% confidence level.

Parameter	Value
E_0 (MeV)	61.70
σ_E (keV)	190.3
$\langle x^2 \rangle^{1/2}$ (mm)	8.251
$\langle \theta_x^2 \rangle^{1/2}$ (mrad)	5.538
$\langle x\theta_x \rangle$ (mm mrad)	33.48
$\langle y^2 \rangle^{1/2}$ (mm)	8.265
$\langle \theta_y^2 \rangle^{1/2}$ (mrad)	5.583
$\langle y\theta_y \rangle$ (mm mrad)	34.13
α_x	-1.077
β_x (mm/mrad)	2.189
ε_x (mm mrad)	31.10
α_y	-1.099
β_y (mm/mrad)	2.200
ε_y (mm mrad)	31.05

Table 9. Parameters of the 63 MeV proton beam at the target plane, obtained by propagating the Gaussian energy spectrum with analytical formulas and the beam ellipses in phase space using FE theory. From top to bottom: mean value E_0 and standard deviation σ_E of the energy spectrum; standard deviations $\langle x^2 \rangle^{1/2}$ and $\langle \theta_x^2 \rangle^{1/2}$, and covariance $\langle x\theta_x \rangle$, of the phase-space diagram for the x-projection; standard deviations $\langle y^2 \rangle^{1/2}$ and $\langle \theta_y^2 \rangle^{1/2}$, and covariance $\langle y\theta_y \rangle$, of the phase-space diagram for the y-projection; Twiss parameters α_x, β_x, and ε_x for the x-projection; Twiss parameters α_y, β_y, and ε_y for the y-projection. Calculated values are rounded to four significant digits.

Parameter	Value
E_0 (MeV)	69.86
σ_E (keV)	221.7
$\langle x^2 \rangle^{1/2}$ (mm)	7.300
$\langle \theta_x^2 \rangle^{1/2}$ (mrad)	4.898
$\langle x\theta_x \rangle$ (mm mrad)	26.15
$\langle y^2 \rangle^{1/2}$ (mm)	7.317
$\langle \theta_y^2 \rangle^{1/2}$ (mrad)	4.941
$\langle y\theta_y \rangle$ (mm mrad)	26.71
α_x	-1.073
β_x (mm/mrad)	2.185
ε_x (mm mrad)	24.38
α_y	-1.096
β_y (mm/mrad)	2.197
ε_y (mm mrad)	24.36

Table 10. Parameters of the 71 MeV proton beam at the target plane, obtained by propagating the Gaussian energy spectrum with analytical formulas and the beam ellipses in phase space using FE theory. From top to bottom: mean value E_0 and standard deviation σ_E of the energy spectrum; standard deviations $\langle x^2 \rangle^{1/2}$ and $\langle \theta_x^2 \rangle^{1/2}$, and covariance $\langle x\theta_x \rangle$, of the phase-space diagram for the x-projection; standard deviations $\langle y^2 \rangle^{1/2}$ and $\langle \theta_y^2 \rangle^{1/2}$, and covariance $\langle y\theta_y \rangle$, of the phase-space diagram for the y-projection; Twiss parameters α_x, β_x, and ε_x for the x-projection; Twiss parameters α_y, β_y, and ε_y for the y-projection. Calculated values are rounded to four significant digits.

Parameter	Value from best fit	Value from covariance matrix
μ (MeV)	70.869 ± 0.001	–
σ (keV)	163.2 ± 0.9	–
λ (MeV^{-1})	6.54 ± 0.09	–
σ_x (mm)	0.7029 ± 0.0009	0.656 ± 0.008
σ_y (mm)	0.6334 ± 0.0008	0.597 ± 0.008
$\langle x^2 \rangle^{1/2}$ (mm)	0.68 ± 0.04	0.656 ± 0.008
$\langle \theta_x^2 \rangle^{1/2}$ (mrad)	2.2 ± 0.1	2.29 ± 0.03
$\langle x\theta_x \rangle$ (mm mrad)	0.679 ± 0.003	0.697 ± 0.009
$\langle y^2 \rangle^{1/2}$ (mm)	0.62 ± 0.03	0.597 ± 0.008
$\langle \theta_y^2 \rangle^{1/2}$ (mrad)	2.3 ± 0.1	2.37 ± 0.03
$\langle y\theta_y \rangle$ (mm mrad)	0.151 ± 0.002	0.274 ± 0.003
α_x	-0.524 ± 0.003	-0.525 ± 0.007
β_x (mm/mrad)	0.352 ± 0.002	0.324 ± 0.004
ε_x (mm mrad)	1.295 ± 0.005	1.33 ± 0.02
α_y	-0.106 ± 0.001	-0.198 ± 0.003
β_y (mm/mrad)	0.271 ± 0.001	0.257 ± 0.003
ε_y (mm mrad)	1.427 ± 0.003	1.39 ± 0.02

Table 11. Parameters of the 71 MeV proton beam propagated up to the first aluminized Mylar foil as obtained by the SRIM simulation of Fig. 11. From top to bottom: parameters μ, σ, and λ of the energy spectrum (EMG fit); standard deviations σ_x and σ_y of the spatial coordinate distribution; standard deviations $\langle x^2 \rangle^{1/2}$ and $\langle \theta_x^2 \rangle^{1/2}$, and covariance $\langle x\theta_x \rangle$, of the phase-space diagram for the x-projection; standard deviations $\langle y^2 \rangle^{1/2}$ and $\langle \theta_y^2 \rangle^{1/2}$, and covariance $\langle y\theta_y \rangle$, of the phase-space diagram for the y-projection; Twiss parameters α_x, β_x, and ε_x for the x-projection; Twiss parameters α_y, β_y, and ε_y for the y-projection. Uncertainties are evaluated at the 95% confidence level.

Parameter	Value from best fit	Value from covariance matrix
μ (MeV)	70.925 ± 0.001	–
σ (keV)	156.3 ± 0.9	–
λ (MeV^{-1})	6.35 ± 0.08	–
σ_x (mm)	0.7629 ± 0.0009	0.713 ± 0.009
σ_y (mm)	0.6941 ± 0.0008	0.653 ± 0.008
$\langle x^2 \rangle^{1/2}$ (mm)	0.74 ± 0.04	0.713 ± 0.009
$\langle \theta_x^2 \rangle^{1/2}$ (mrad)	2.9 ± 0.2	3.02 ± 0.04
$\langle x\theta_x \rangle$ (mm mrad)	1.221 ± 0.005	1.21 ± 0.02
$\langle y^2 \rangle^{1/2}$ (mm)	0.70 ± 0.04	0.653 ± 0.008
$\langle \theta_y^2 \rangle^{1/2}$ (mrad)	3.1 ± 02	2.96 ± 0.04
$\langle y\theta_y \rangle$ (mm mrad)	0.732 ± 0.003	0.76 ± 0.01
α_x	-0.678 ± 0.004	-0.681 ± 0.009
β_x (mm/mrad)	0.307 ± 0.002	0.286 ± 0.004
ε_x (mm mrad)	1.800 ± 0.007	1.78 ± 0.02
α_y	-0.367 ± 0.002	-0.429 ± 0.005
β_y (mm/mrad)	0.2428 ± 0.0009	0.240 ± 0.003
ε_y (mm mrad)	1.995 ± 0.005	1.78 ± 0.02

Table 12. Parameters of the 71 MeV proton beam propagated up to the first aluminized Mylar foil as obtained by the FLUKA simulation of Fig. 12. From top to bottom: parameters μ, σ, and λ of the energy spectrum (EMG fit); standard deviations σ_x and σ_y of the spatial coordinate distribution; standard deviations $\langle x^2 \rangle^{1/2}$ and $\langle \theta_x^2 \rangle^{1/2}$, and covariance $\langle x\theta_x \rangle$, of the phase-space diagram for the x-projection; standard deviations $\langle y^2 \rangle^{1/2}$ and $\langle \theta_y^2 \rangle^{1/2}$, and covariance $\langle y\theta_y \rangle$, of the phase-space diagram for the y-projection; Twiss parameters α_x, β_x, and ε_x for the x-projection; Twiss parameters α_y, β_y, and ε_y for the y-projection. Uncertainties are evaluated at the 95% confidence level.

Parameter	Value
E_0 (MeV)	70.80
σ_E (keV)	198.9
$\langle x^2 \rangle^{1/2}$ (mm)	0.7149
$\langle \theta_x^2 \rangle^{1/2}$ (mrad)	2.717
$\langle x\theta_x \rangle$ (mm mrad)	1.071
$\langle y^2 \rangle^{1/2}$ (mm)	0.6537
$\langle \theta_y^2 \rangle^{1/2}$ (mrad)	2.793
$\langle y\theta_y \rangle$ (mm mrad)	0.6572
α_x	-0.6611
β_x (mm/mrad)	0.3155
ε_x (mm mrad)	1.620
α_y	-0.3859
β_y (mm/mrad)	0.2509
ε_y (mm mrad)	1.703

Table 13. Parameters of the 71 MeV proton beam propagated up to the first aluminized Mylar foil, obtained by propagating the Gaussian energy spectrum with analytical formulas and the beam ellipses in phase space using FE theory. From top to bottom: mean value E_0 and standard deviation σ_E of the energy spectrum; standard deviations $\langle x^2 \rangle^{1/2}$ and $\langle \theta_x^2 \rangle^{1/2}$, and covariance $\langle x\theta_x \rangle$, of the phase-space diagram for the x-projection; standard deviations $\langle y^2 \rangle^{1/2}$ and $\langle \theta_y^2 \rangle^{1/2}$, and covariance $\langle y\theta_y \rangle$, of the phase-space diagram for the y-projection; Twiss parameters α_x, β_x, and ε_x for the x-projection; Twiss parameters α_y, β_y, and ε_y for the y-projection. Calculated values are rounded to four significant digits.

Profile type	σ_x (mm)	σ_y (mm)
EBT3	13.69 ± 0.03	13.54 ± 0.03
SRIM	7.84 ± 0.02	8.09 ± 0.03
FLUKA	12.51 ± 0.04	12.36 ± 0.03
Fermi-Eyges	12.05	12.03

Table 14. Standard deviations of the beam profiles shown in Fig. 14. Excluding the analytically calculated values for the FE Gaussian profiles, the standard deviations of the other cases are obtained from Gaussian best fits of the profiles.

References

Ahdi2022 C. Ahdida, D. Bozzato, D. Calzolari, F. Cerutti, N. Charitonidis, A. Cimmino, A. Coronetti, G. L. D'Alessandro, A. Donadon Servelle, L.S. Esposito, R. Froeschl, R. García Alía, A. Gerbershagen, S. Gilardoni, D. Horváth, G. Hugo, A. Infantino, V. Kouskoura, A. Lechner, B. Lefebvre, G. Lerner, M. Magistris, A. Manousos, G. Moryc, F. Ogallar Ruiz, F. Pozzi, D. Prelipcean, S. Roesler, R. Rossi, M. Sabaté Gilarte, F. Salvat Pujol, P. Schoofs, V. Stránský, C. Theis, A. Tsinganis, R. Versaci, V. Vlachoudis, A. Waets, M. Widorski, *New capabilities of the FLUKA multi-purpose code*, Front. Phys. **9** (2022) 788253.

Andr2021 E.G. Androulakaki, M. Kokkoris, M. Mayer, E. Mitsi, N. Patronis, E. Vagena, *A comparative study of multiple scattering calculations implemented in general-purpose Monte Carlo and selected ion beam analysis codes*, Nucl. Instrum. Phys. Res. B **496** (2021) 71-77.

Ashl2025 Website of Ashland: https://www.ashland.com/industries/medical/radiotherapy-films.

Batt2015 G. Battistoni, T. Boehlen, F. Cerutti, P.W. Chin, L.S. Esposito, A. Fassò, A. Ferrari, A. Lechner, A. Empl, A. Mairani, A. Mereghetti, P.G. Ortega, J. Ranft, S. Roesler, P.R. Sala, V. Vlachoudis, G. Smirnov, *Overview of the FLUKA code*, Ann. Nucl. Energy **82** (2015) 10-18.

Beth1953 H.A. Bethe, *Molière's theory of multiple scattering*, Phys. Rev. **89** (1953) 1256-1266.

Böhl2014 T.T. Böhlen, F. Cerutti, M.P.W. Chin, A. Fassò, A. Ferrari, P.G. Ortega, A. Mairani, P.R. Sala, G. Smirnov, V. Vlachoudis, *The FLUKA Code: Developments and Challenges for High Energy and Medical Applications*, Nucl. Data Sheets **120** (2014) 211-214.

Camp2017 L. Campajola, P. Casolaro, F. Di Capua, *Absolute dose calibration of EBT3 Gafchromic films*, J. Instrum. **12** (2017) P08015.

Caso2019 P. Casolaro, L. Campajola, F. Di Capua, *The physics of radiochromic process: one calibration equation for all film types*, J. Instrum. **14** (2019) P08006.

Cran1994 K.R. Crandall, M. Weiss, TERA 94/34 ACC 20, internal note (1994).

Eyge1948 L. Eyges, *Multiple scattering with energy loss*, Phys. Rev. **74** (1948) 1534-1535.

Ferr2005 A. Ferrari, P.R. Sala, A. Fassò, J. Ranft, *FLUKA: a multi-particle transport code*, CERN-2005-10 (2005), INFN/TC_05/11, SLAC-R-773.

Fluk2025 Website of FLUKA software (CERN version): https://fluka.cern.

Fluk2025b Website of FLUKA software (INFN version): http://www.fluka.org/fluka.php.

Gott2010 B. Gottschalk, *On the scattering power of radiotherapy protons*, Med. Phys. **37** (2010) 352-367.

Gott2012 B. Gottschalk, *Techniques of proton radiotherapy: transport theory*, arXiv:1204.4470 [physics.med-ph] (2012) 1-43.

Math2025 Wolfram Research, Inc., Mathematica, v. 14.2, Champaign, Illinois (2025). Website: https://www.wolfram.com/mathematica.

Matl2010 MathWorks MATLAB, v. 7.10.0 (R2010a), The MathWorks Inc., Natick, Massachusetts (2010). Website: https://www.mathworks.com.

Moli1947 G. Molière, *Theorie der Streuung schneller geladener Teilchen I Einzelstreuung am abgeschirmten Coulomb-Feld*, Z. Naturforschg. **2a** (1947) 133-145.

Moli1948 G. Molière, *Theorie der Streuung schneller geladener Teilchen II Mehrfach- und Vielfachstreuung*, Z. Naturforschg. **3a** (1948) 78-97.

Nenz2022 P. Nenzi, A. Ampollini, M.D. Astorino, G. Bazzano, F. Fortini, L. Picardi, C. Ronsivalle, V. Surrenti, E. Trinca, *Status of the TOP-IMPLART proton linac*, Proceedings of the LINAC2022 Conference, Liverpool UK (2022), p. 138.

Nich2024 E. Nichelatti, M. Piccinini, A. Ampollini, M.D. Astorino, G. Bazzano, P. Nenzi, V. Surrenti, E. Trinca, C. Ronsivalle, *Approximate calculation of backpropagated energy spectrum for a proton beam*, J. Appl. Phys. **136** (2024) 244901.

Pica2020 L. Picardi, A. Ampollini, G. Bazzano, E. Cisbani, F. Ghio, R.M. Montereali, P. Nenzi, M. Piccinini, C. Ronsivalle, F. Santavenere, V. Surrenti, E. Trinca, M. Vadrucci, E. Wembe Tafo, *Beam commissioning of the 35 MeV section in an intensity modulated proton linear accelerator for proton therapy*, Phys. Rev. Accel. Beams **23** (2020) 020102.

Rons2011 C. Ronsivalle, M. Carpanese, C. Marino, G. Messina, L. Picardi, S. Sandri, E. Basile, B. Caccia, D.M. Castelluccio, E. Cisbani, S. Frullani, F. Ghio, V. Macellari, M. Benassi, M. D'Andrea, L. Strigari, *The TOP-IMPLART Project*, Eur. Phys. J. Plus **126** (2011) 68.

Ross1941 B. Rossi, K. Greisen, *Cosmic-ray theory*, Rev. Mod. Phys. **12** (1941) 240-309.

Srim2013 Website of SRIM software: http://www.srim.org.

Surr2023 V. Surrenti, A. Ampollini, M.D. Astorino, G. Bazzano, F. Fortini, P. Nenzi, L. Picardi, C. Ronsivalle, E. Trinca, *The new proton beam delivery line of the TOP-IMPLART accelerator*, Proceedings of IPAC23 Conference, Venice, IT (2023), p. 2423.

Vlac2009 V. Vlachoudis, *FLAIR: A powerful but user friendly graphical interface for FLUKA*, in Proceedings of International Conference on Mathematics, Computational Methods & Reactor Physics (M&C 2009), New York (Saratoga Springs, 2009).

Wied2015 H. Wiedemann, *Particle Accelerator Physics*, 4th ed., Springer (New York, USA), 2015.

Zieg2008 J.F. Ziegler, J.P. Biersack, M.D. Ziegler, *The Stopping and Range of Ions in Matter*, SRIM Co. (Chester, Maryland, USA), 2008.

Zieg2010 J.F. Ziegler, M.D. Ziegler, J.P. Biersack, *SRIM – the stopping and range of ions in matter*, Nucl. Instrum. Methods Phys. Res. B **268** (2010) 1818–1823.

ENEA
Servizio Promozione e Comunicazione
www.enea.it

Stampa: Laboratorio Tecnografico ENEA - C.R. Frascati
maggio 2025